Structural evolution, exhumation rates, and rheology of the European crust during Alpine collision: constraints from the Rotondo granite – Gotthard nappe

A. Ceccato[1], W. M. Behr[1], A. S. Zappone[2], L. Tavazzani[3], and A. Giuliani[3]

[1]Structural Geology and Tectonics Group, Geological Institute, Department of Earth Sciences, ETH Zurich, Sonneggstrasse 5, 8092 Zurich, Switzerland.

[2]Swiss Seismological Service, ETHZ, Zurich, 8092, Switzerland.

[3]Institute of Geochemistry and Petrology, Department of Earth Sciences, ETH Zurich, Clausiusstrasse 25, 8092 Zurich, Switzerland.

Corresponding author: Alberto Ceccato (aceccato@erdw.ethz.ch)

Key Points:

- Garnet U-Pb, mica Rb-Sr dating constrain exhumation of Rotondo granite from amphibolite facies at 34-20 Ma to greenschist facies at 15-14 Ma
- Fast exhumation (1-3 mm/yr) accommodated by ductile shearing of weak shear zones localized on pre-collisional brittle deformation structures
- The European crust was extremely weak during collision, rheology was controlled by metamorphic and fluid evolution in localized shear zones

Abstract

The rheology of crystalline units controls the large-scale deformation geometry and dynamics of collisional orogens. Defining a time-constrained rheological evolution of such units may help unravel the details of collisional dynamics. Here, we integrate field analysis, pseudosection calculations and in-situ garnet U-Pb and mica Rb-Sr geochronology to define the structural and rheological evolution of the Rotondo granite (Gotthard nappe, Central Alps). We identify a sequence of four (D_1-D_4) deformation stages. Pre-collisional D_1 brittle faults developed before Alpine peak metamorphism, which occurred at 34-20 Ma (U-Pb garnet ages) at 590 ± 25ºC and 0.95 ± 0.1 GPa. The reactivation of D_1 structures controlled the rheological evolution, from D_2 reverse mylonitic shearing at amphibolite facies (520 ± 40ºC and 0.85 ± 0.1 GPa) at 18-20 Ma (white mica Rb-Sr ages), to strike-slip, brittle-ductile shearing at greenschist-facies D_3 (395 ± 25 ºC and 0.4 ± 0.1 GPa) at 14-15 Ma (white and dark mica Rb-Sr ages), and then to D_4 strike-slip faulting at shallow conditions. Although highly misoriented for the Alpine collisional stress orientation, D_1 brittle structures controlled the localization of D_2 ductile mylonites accommodating fast (1-3 mm/yr) exhumation rates due to their weak shear strength (<10 MPa). This structural and rheological evolution is common across External Crystalline Massifs (e.g., Aar, Mont Blanc), suggesting that the entire European crust was extremely weak during Alpine collision, its strength controlled by weak ductile shear zones localized on pre-collisional deformation structures, that in turn controlled localized exhumation at the scale of the orogen.

1 Introduction

During mountain-building events, rheological contrasts between lithospheric plates are first-order controls on the geometry of collision (Faccenda et al., 2008; Vogt et al., 2018, Candioti et al., 2021), the development of topography (Cook & Royden, 2008; Wolf et al., 2022), and the styles and rates of regional deformation and metamorphism (Willingshofer et al., 2005; Piccolo et al., 2018). Rheological contrasts may result from different crustal compositions, ages, geological histories, and/or thermal regimes of the lithospheric plates involved in collision (Audet & Burgmann, 2011; Mouthereau et al., 2013). For example, depending on the composition and the fluid content, lithospheric plates may present different mechanical behavior (brittle vs. viscous deformation) and strength at the same depth and temperature conditions during collision (Bürgmann & Dresen, 2008; Menegon et al., 2011; Behr & Platt, 2014, Jamtveit et al., 2019). Furthermore, the occurrence of anisotropic structural fabrics (foliations and fractures), strictly related to the geological history of crustal sections, may promote or hinder deformation depending on their suitability to be reactivated, and/or their ability to promote or hinder fluid infiltration (Ceccato et al., 2020, Zertani et al., 2023). Pressure, temperature, fluid, and structural fabrics evolve with the tectono-metamorphic evolution of a collisional orogen, and so does their effects on the rheological contrast between colliding plates (Groome et al., 2008; Behr & Platt, 2013; Bellanger et al., 2014; Ceccato et al., 2020).

Most of the deformation and shortening in the core of collisional belts is accommodated through deformation of crystalline basement units (Lacombe & Mouthereau, 2002; Rosenberg & Kissling, 2013; Pfiffner, 2016). Such crystalline units are typically characterized by poly-metamorphic histories, with wet and/or dry mineral assemblages, and multiple tectonic fabrics, all of them strongly affecting the rheology during collision (Audet & Burgmann, 2011;

Moutherau et al., 2013). Moreover, pre-collisional events such as lithospheric rifting, prograde burial, and subduction, lead to the development of additional deformation structures (e.g., rift-related normal fault zones) and tectonic fabrics (e.g., prograde foliations), which may introduce rheological heterogeneity that later influences collisional dynamics (Mohn et al., 2014). The European Alps is a region where both inherited compositional and fabric variations, as well as pre-collisional tectonics, are thought to have strongly influenced later syn-orogenic development. For example, rheological contrast between the upper (Adriatic) and lower (European) crust varies along the strike of the orogen, and resulted in different patterns of strain partitioning, amounts of shortening and exhumation, and collisional styles between the Western, Central and Eastern Alps (Bellahsen et al., 2014; Rosenberg & Kissling, 2013). In the Central Alps, in particular, the Adriatic upper plate indents into the weaker, thickened European crust (Rosenberg & Kissling, 2013). The European thickened crust is composed of stacked slices of crystalline basement derived from the thinned Mesozoic European margin, now exposed in the Aar massif, Gotthard nappe, and Lepontine dome (Fig. 1). The thickened European crust is considered here to be much weaker than the juxtaposed Adriatic continental lithosphere, represented by the almost undeformed, lower-crustal Ivrea-Verbano complex (Fig. 1). However, constraints on the factors controlling this "weakness" are sparse, including whether the crust was weak since the beginning of burial and subduction, or if it was initially strong and then progressively weakened during collision. Both tectonic inheritance related to Mesozoic rifting (Bellahsen et al., 2014) and syn-collisional Barrovian metamorphism (Rosenberg & Kissling, 2013) might have contributed to the weakening of the European continental crust in this part of the Alps.

To better understand this weakening process, and the extent to which different factors (temperature, fluids, inherited fabrics) contributed to it, a detailed characterization of the structural and rheological evolution of the crystalline basement is required. Providing a time-integrated evolution of the rheology and of the geological parameters controlling this evolution might help us to quantitatively constrain the relationship between the rheology of crystalline basement units and the large-scale geometry and dynamics of the Alpine orogen.

In this regard, previous investigations have revealed a recurrent brittle-to-ductile structural evolution (i.e., ductile shear zone related to collisional processes overprinting pre-existent brittle faults and fractures) of crystalline basement units in the Western and Central Alps (e.g., Mont Blanc: Guermani & Pennacchioni, 1998; Gran Paradiso: Menegon & Pennacchioni, 2010; Aar-Gotthard: Oliot et al., 2014; Rolland et al., 2009; Wehrens et al., 2016; Lepontine Dome: Goncalves et al., 2016). Several hypotheses were proposed to explain such brittle-to-ductile evolution, including the occurrence of prograde brittle deformation during burial (Guermani & Pennacchioni, 1998), and mid-crustal seismicity at peak metamorphic conditions (Wehrens et al., 2016). Previous authors have also speculated on the occurrence of pervasive extensional faulting related to the Mesozoic rifting of the European margin, providing field evidence for limited reactivation of structures inherited from rifting (Ballèvre et al., 2018; Dall'Asta et al., 2022; Herwegh et al., 2017, 2020; Nibourel et al. 2021; Musso-Piantelli et al., 2022).

Here we present an integrated field and petrochronological study of the deformation features of the Rotondo granite in the Gotthard nappe (Fig. 1). The Gotthard nappe represents a sliver of European crust now exposed in the Central Swiss Alps. The Rotondo granite is a Post-Variscan pluton (i.e., not affected by Variscan tectonometamorphic events), intruded into the European polymetamorphic crust. Differently from its host polymetamorphic host rock, the lack

of Variscan pervasive fabrics (foliations) and the homogeneous texture of the granite allow us to define a sequence of (localized) deformation structures probably related to Alpine deformation. We use structural and petrochronological data to:

i. Define the pressure-temperature-time-deformation (*P-T-t-d*) path of the Rotondo granite;
ii. Examine the time-constrained structural and rheological evolution of the thickened crust of the lower plate during Alpine continental collision;
iii. Investigate the geological factors that affect the rheological evolution of the crystalline unit.

2 Geological setting

The European Alps (Fig. 1) are a double-verging orogen resulting from the continental collision between Europe and Adria, following the closure and subduction of the Mesozoic Tethys ocean (Dal Piaz et al., 2003). European and Adriatic polymetamorphic crustal sections were each strongly modified by the Variscan orogeny during the formation of the Pangean supercontinent. The Permo-Mesozoic breakup of Pangea led to the development of the Tethys Ocean, including the Liguro-Piemontese ocean and Valais trough. The development of the Liguro-Piemontese ocean divided Europe from Adria (210-140 Ma) by 200-400 km (Ballèvre et al., 2018; Beltrando et al., 2014). A second, more short-lived rifting phase took place on the European margin to the north of the Liguro-Piemontese ocean and led to the development of the Valais trough during Late-Jurassic to Early Cretaceous (140-120 Ma), separating the European distal margin from the southern Briançonnais microcontinent (Beltrando et al., 2012; Célini et al., 2023; Handy et al., 2010). This former paleogeography is now preserved in the Internal (Penninic) domains of the Central and Western Alps, exposing the remnants of the Valaisan, Briançonnais and Liguro-Piemontese units (Fig. 1). The proximal European passive margin is now exposed in the External Crystalline Massifs (ECMs), including: Aar, Mont Blanc, Aiguille Rouges, Belledonne, Pelvoux-Oisian massifs as well as in the Gotthard nappe (Fig. 1a; Lemoine et al., 1986).

The study area is located in the Gotthard nappe (Swiss Alps, Fig. 1a). The Gotthard nappe includes a series of polymetamorphic Ordovician-Silurian crystalline units intruded by late-Variscan granitoids (Berger et a., 2017). The crystalline units include high-grade gneisses of the Val Nalps, Paradis and Streifegneis complexes (Fig. 2a; Berger et al., 2017). The Val Nalps and Paradis Complexes preserve evidence of an Early- to Mid-Ordovician (~470 Ma) high grade metamorphism, later affected by Silurian (~440 Ma) magmatism (Berger et al., 2017). Between 340 and 300 Ma, these complexes were affected by Variscan amphibolite facies metamorphism and transpressional shearing (Bühler et al., 2022; Simonetti et al., 2020; Vanardois et al., 2022). Post-Variscan magmatism led to the intrusion of several granitic plutons into the polymetamorphic basement, including the Cristallina granodiorite, the Fibbia and Gamsboden granite-gneisses and the Rotondo granite (Fig., 1b; Berger et al., 2017).

At the regional scale, the European crust was affected by the development of Permo-Mesozoic transtensional basins, resulting eventually in the formation of the Valais trough in the Jurassic-Cretaceous period (Ballèvre et al., 2018; Célini et al., 2023; Handy et al., 2010). The units now included in the Gotthard nappe were part of the distal European passive margin located north of the Valais trough (Schmid et al., 2004). From the Late Cretaceous onwards, convergence between Europe and Adria led to the subduction of the Liguro-Piemontese ocean

and to progressive development of the Penninic accretionary wedge facing the advancing Adriatic upper plate (Dal Piaz et al., 2003). Progressive convergence led to burial and underthrusting of the European passive margin, eventually leading to continental collision. The Gotthard nappe was buried beneath the advancing Penninic accretionary wedge around 35 Ma (Handy et al., 2010), reaching greenschist-facies conditions between 35 and 22 Ma (Herwegh et al., 2020; Janots et al., 2009). Subsequently, continental collision between Europe and Adria led to the rapid exhumation of the crystalline units of the Gotthard-Aar massifs at around 22-17 Ma, through the activation of greenschist facies sub-vertical ductile shear zones with reverse kinematics (T = 450-500 ºC and P = 0.7-0.8 GPa; Challandes et al., 2008; Goncalves et al., 2012; Herwegh et al., 2017; Oliot et al., 2010; Rolland et al., 2008, 2009). From 14 Ma onward, the Gotthard nappe was then affected by regional strike-slip tectonics related to the activity of the Simplon-Rhone transtensional fault system (Campani et al., 2010; Herwegh et al., 2017). Shallow brittle faulting has affected the Gotthard nappe since the Late Miocene, leading to the activation of brittle gouge-bearing faults up to recent times (Kralik et al., 1992; Pleuger et al., 2012).

2.1 The Rotondo granite

The Rotondo Granite (RG) is an Early-Permian (295 Ma, U-Pb on zircon, Rast et al., 2022) peraluminous granite, crosscut by mafic dykes (290-285 Ma, U-Pb on zircon, Bussien et al., 2008). It includes two main magmatic facies (equigranular RG_1 and porphyritic RG_2) both composed of Qz + Kfs + Pl + Bt ± Wm ± Grt ± Ep ± Chl ± Zr ± Spn ± Cal ± Py (Rast et al., 2022, mineral abbreviations from Whitney & Evans, 2010; Wm: white mica). RG_1 and RG_2 facies only differ by mineral proportions and the occurrence of a Bt-Kfs foliation in RG_2 (Rast et al., 2022). This meso-scale bulk foliation has been attributed to an Alpine greenschist facies overprint, based on field and microstructural observations (Gapais et al., 1987; Steck, 1976; Steck & Burri, 1971). Another evidence of Alpine greenschist facies metamorphism is the occurrence of atoll-like garnets in the Rotondo granite (Steck, 1976; Steck & Burri, 1971). The peculiar atoll-like shape, and their Ca-rich composition, have been interpreted by Steck & Burri (1971) to reflect two metamorphic growth stages at different temperature and/or fluid activity conditions. However, the textural relationship between the atoll-garnets and the bulk foliation was not addressed in detail. A set of steep, NW-dipping ductile shear zones, with top-to-SE dip-slip reverse kinematics developed during the same Alpine retrograde event (Lützenkirchen & Loew, 2011). The ductile shear zones have been classified in two main groups (Rast et al., 2022): (i) granitic shear zones, composed of fine-grained mylonite with feldspar augens in a biotite-bearing foliation; and (ii) quartz-biotite-rich shear zones, characterized by the occurrence of sigmoidal quartz veins with rigid cm-sized calcite clasts. Ductile shear zones were exploited as nucleation sites for late brittle faulting at upper crustal levels, as inferred from the stability of syn- to post-kinematic zeolite minerals, and the formation of clay-rich gouges (Lützenkirchen & Loew, 2011). Despite the general understanding of the regional and local scale tectonic evolution, a detailed and holistic description of the structural and tectonometamorphic features, and absolute timing of deformation events in this area are still missing.

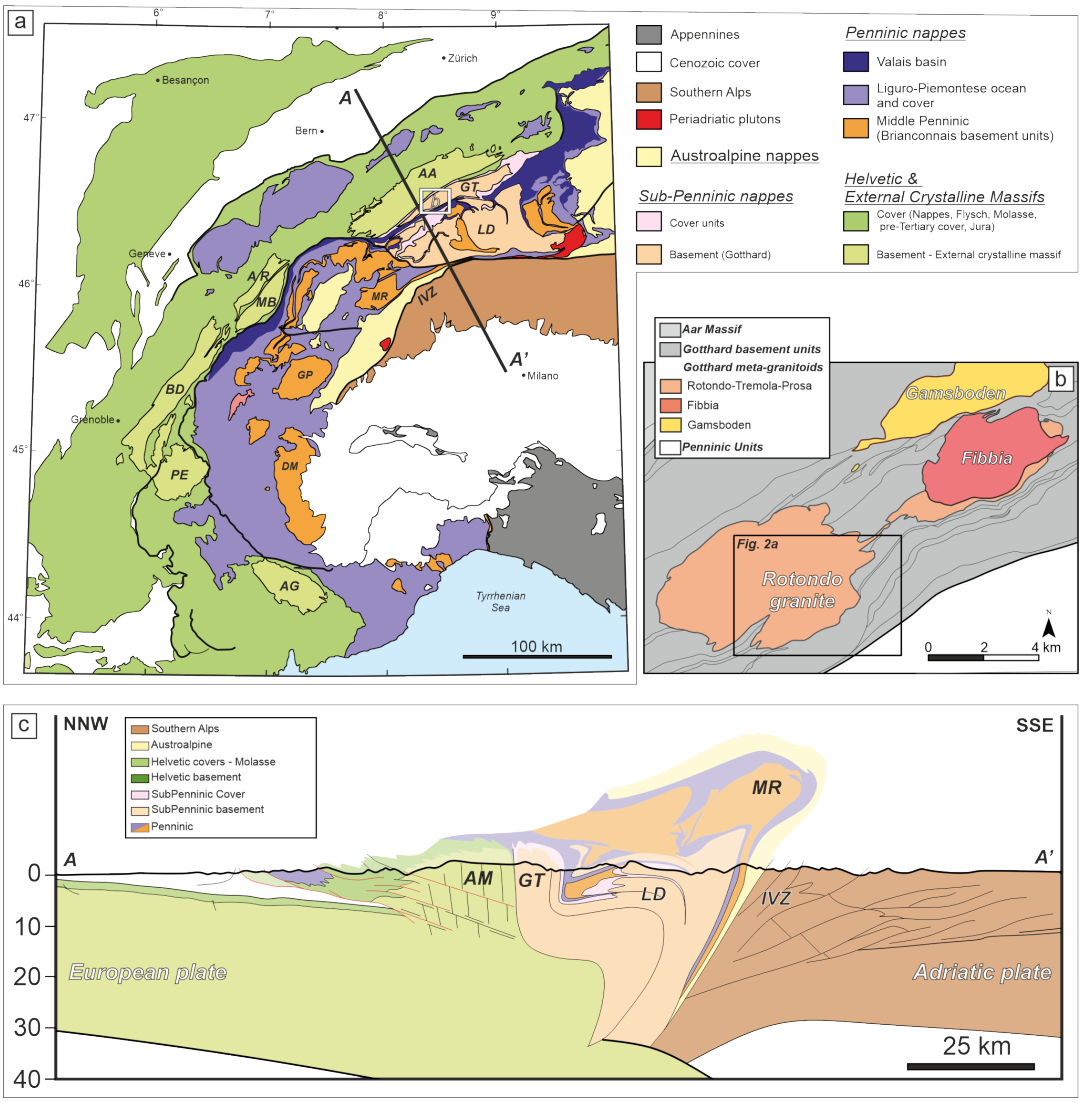

Figure 1: Geological setting of the study area. (a) Tectonic sketch of the Central-Western Alps (redrawn from Ballèvre et al., 2018, Schmid et al., 2004). AA: Aar; AG: Argentera; AR: Aiguilles rouges; BD: Belledonne; DM: Dora Maira; GP: Gran Paradiso; GT: Gotthard; IVZ: Ivrea-Verbano Zone; LD: Lepontine Dome; MB: Mont Blanc; MR: Monte Rosa; PE: Pelvoux. (b) Tectonic sketch of the Central-Western Gotthard massif showing the spatial distribution of the meta-granitoid intrusion (Rotondo, Fiabbia, Gamsboden). (c) Geological section across the Central Swiss Alps.

3 Material and Methods

3.1. Field structural analysis

This work further extends the previous work of Lützenkirchen & Loew (2011) and Rast et al. (2022), improving the detail of structural description, and adding absolute age constraints on the deformation structures, with implications on regional tectonic and rheological evolution. It provides a detailed description of the structural evolution and inventory of the deformation structures affecting the rock massif hosting the Bedretto Underground Laboratory for

Geosciences and Geoenergies (BULGG; Ma et al., 2022). Field survey was focused on the analyses of deformation features and the collection of structural data at 205 structural stations ("Waypoints" – WP in Fig. 2a), resulting in a georeferenced dataset of 473 structural measurements, each of which includes a structural description, orientation of shear plane (Dip/Dip direction) and lineation (Trend/Plunge), kinematics, mineralogy, deformation fabric (brittle vs. ductile), thickness, length, and throw. These structures were then subdivided into sets based on kinematic compatibility, mineralogy, and texture. Oriented samples were collected for further microstructural and petrochronological analysis. The geographic coordinates of relevant waypoints are reported in the Supplementary Information (SI) Table S1. The Structural dataset is available in the SI Dataset DS1

3.2. Optical/Scanning Electron Microscopy and Electron Probe Micro Analyses

Thin sections were cut parallel to the lineation direction (X kinematic direction) and perpendicular to the foliation plane (XY kinematic plane). Backscattered electron (BSE) images and Energy Dispersion Spectrometry (EDS) mapping were performed at ScopeM (ETH) with a Hitachi SU5000 Scanning Electron Microscope (SEM). Quantitative compositional analyses were performed at the Institute for Geochemistry and Petrology (ETH) with a JEOL JXA-8230 Electron Probe Microanalyzer equipped with five Wavelength Dispersion Spectrometers (WDS). Further details on analytical conditions are reported in the SI Text S1. Mineral compositions are reported in the SI Table S2.

3.3. P-T pseudosection calculation

The bulk rock compositions adopted for pseudosection calculation were obtained by X-Ray Fluorescence spectroscopy at the Institute for Geochemistry and Petrology (ETH) with a WD-XRF PANalytical AXIOS equipped with five diffraction crystals (bulk compositions are reported in the SI Table S3). Pressure-temperature pseudosection calculations were performed with Perple_X 6.9.1 (Connolly, 2005) adopting the thermodynamic database of pure end-members from Holland & Powell, (2011; hp62ver.dat). Adopted solid solution models and computational details are reported in the SI Text S1. The chemical system used for the calculation is MnO-Na_2O-CaO-K_2O-FeO-MgO-Al_2O_3-SiO_2-H_2O-TiO_2-Fe_2O_3 (MNCKFMASHTO). In the text, the term "observed" refers to the paragenesis observed in thin section and to the phase chemistry obtained from EPMA analyses; the term "computed" refers to the chemistry and mineral paragenesis calculated by pseudosection computations. Results of pseudosections and related files are available in the SI Dataset DS2.

3.4. In-situ LA-ICP-MS U-Pb & Trace Element analyses

In-situ Garnet U-Pb dating, and trace element analyses were performed on polished thin sections by laser ablation-inductively coupled plasma-mass spectrometry (LA-ICP-MS) at the ERDW department of ETH Zurich using an ASI RESOlution S-155 excimer (ArF, 193 nm) laser ablation system coupled to a Thermo Scientific Element XR sector-field ICP-MS (Guillong et al., 2014). Instrumentation and data acquisition parameters for U-Pb dating are summarized in SI Dataset DS3 reporting standards of Horstwood et al. (2016). All data from the session, including details on the data reduction strategies and results of validation reference materials can be found in SI Dataset DS3.

3.5. In-situ LA-ICP-MS Rb-Sr analyses

In situ Rb-Sr isotope analyses of mica in thin section were undertaken using an ASI RESOlution 193 nm excimer laser probe interfaced to an Agilent 8800 ICP-MS/MS at ETH Zurich following the procedure outlined in Giuliani et al. (2023). This method employs an isochronous in-house mica reference material from the Wimbledon lamproite (Sarkar et al., 2023) to calibrate the Rb/Sr fractionation in mica unknowns following initial calibration of $^{87}Sr/^{86}Sr$ and $^{87}Rb/^{86}Sr$ using the silicate glass reference material NIST 610. This method is validated by analyses of micas from the Bultfontein kimberlite with ages independently constrained by isotope-dilution Rb-Sr dating (Fitzpayne et al., 2020). All the details pertaining analytical conditions, reference materials and data processing can be found in the SI Text S1. The Rb-Sr age data are summarized in Table 1 and all the Rb-Sr analyses can be found in SI Dataset DS4.

4. Results

4.1 Field observations – Sequence of localized deformation structures

In the following, we describe the sequence of subsolidus deformation structures, numbered following their relative chronology (from the oldest D_1, to the youngest D_4), as inferred from field analyses of crosscutting and overprinting relationships, mineralogy, texture, and kinematics. Structural data are summarized in Fig. 2b-i. Field images of the described structure sets are reported in Figs. 3-4-5. In the SI Text S2, additional data about the magmatic structures (aplitic and mafic dykes), and the tectonometamorphic evolution of the RG-host rocks are presented.

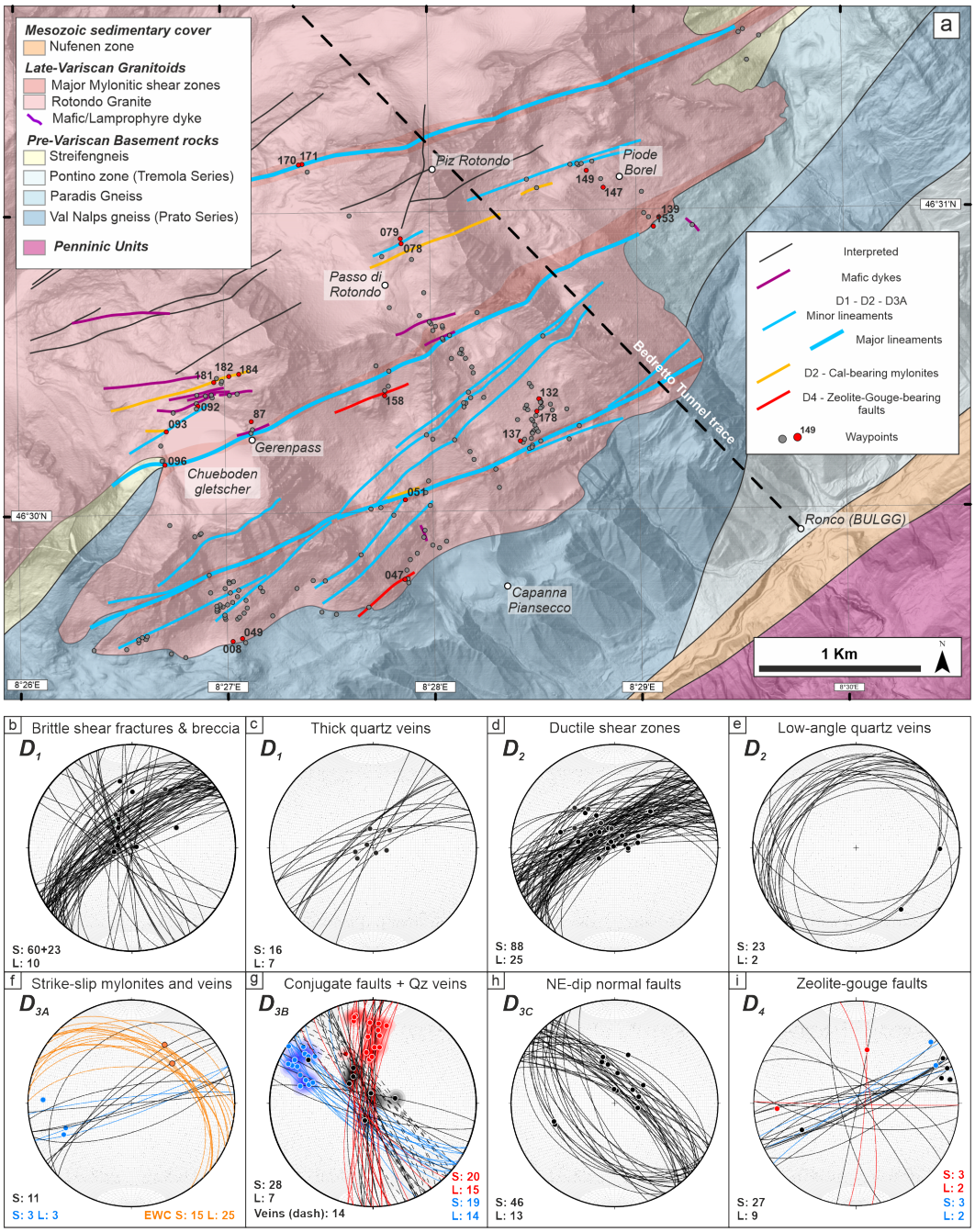

Figure 2. Structural map and data of the surveyed area in the Rotondo granite. (a) Structural field map of the southern rim of the Rotondo Granite summarizing the field observations and showing the location of investigated areas (modified after Berger et al., 2017). (b-i) Equal area, lower-hemisphere stereographic projections of the structural data for each set of deformation structures. Great circles: slip planes (S); Dots and contour: lineations (L). Blue and red planes and dots represent dextral and sinistral kinematics, respectively. Contours are calculated as Area percentage, minimum contour is 5 area% - computed with Stereonet 11 (https://www.rickallmendinger.net/stereonet). (b) D_1 shear fractures, cataclasites and breccias;

(c) D_1 plane-parallel thick quartz veins; (d) D_2 ductile shear zones, dip-slip, top-to-SE reverse kinematics; (e) low-angle quartz veins kinematically related to D_2 shear zones; (f) D_{3A} ductile shear zones (black great circles) showing strike-slip reactivation and associated extensional wing cracks (EWC) and quartz-veins developed in dilational jogs (orange great circles); (g) D_{3B} conjugate, brittle-ductile shear zones (solid great circles) and extensional veins (dashed great circles); (h) D_{3C} normal faults; (i) D_4 Zeolite- and gouge-bearing brittle fault zones.

4.1.1. D_1 brittle shear fractures, cataclasites and breccias

The D_1 set consists of brittle shear fractures (Fig 3a), cataclasites (Fig. 3b) and breccias (Fig. 3c-d) containing a dark, fine-grained matrix that surrounds angular clasts of undeformed granite (Fig. 3c-d). Milky quartz veins are common along these structures, ranging in thickness from a few mm (Fig. 3e), to >1 m (Fig. 3e-f), and showing mutual overprinting relationship with the dark fine-grained matrix (Fig. 3e-h). In some cases, large breccia bodies are observed, characterized by a transitional texture from crackle-breccias to fine grained cataclasites. A peculiar feature of D_1 structures is the occurrence of mm-size garnets overgrowing the dark matrix (Fig. 3b,c,d,g). D_1 structures are steeply dipping, SE-verging, and ENE-WSW-striking (Fig. 2b-c). A subset of D_1 cataclasites (23 planar measurements) presents an orientation at high angle to the main set (Fig. 2b). The kinematics of set D_1 structures is rather difficult to constrain, given that they are overprinted by the following stage of ductile deformation. A dip-slip lineation L_1 is observed on the exposed surface of the matrix (Fig. 3g), and incipient breccias and shear fractures commonly show either strike-slip dextral or normal-sense displacement of crosscut markers in the present orientation (Fig. 3h). Garnet is only observed in D_1 structures not heavily overprinted by the ductile deformation related to D_2 shear zones (Fig. 3b-c).

4.1.2. D_2 Dip-slip, reverse ductile shear zones

The D_2 set consists of mylonitic ductile shear zones. D_2 shear zones exploit as nucleation site the pre-existing structural and/or compositional heterogeneities in the host Rotondo granite, such as aplitic and mafic dykes, veins, and D_1 structures (Fig. 4). Deformed aplitic and mafic dykes develop an oblique homogeneous foliation abruptly terminating at the dyke selvage against the undeformed host RG. D_2 shear zones exploiting D_1 brittle structures preserve the geometric and textural complexity of the precursor, developing an heterogeneous Bt-Wm-bearing foliation wrapping around low-strain granite clasts and lithons (Fig. 4b). D2 structures strike ENE-WSW, showing a dip-slip, L_2 Bt-Wm-bearing lineation (Fig. 2d). The dominant kinematics is reverse, top-to-SE, even though dip-slip normal kinematics are observed on rare SE-steeply-dipping shear planes. Overall, the D_2 ductile shear zones form a large-scale network defined by subparallel zones of high strain surrounding high-aspect-ratio lozenges of undeformed granite (Gapais et al., 1987). Sheared quartz + calcite veins are common in high strain D_2 ductile shear zones (Fig. 4a; see also Fig. 11 of Rast et al. 2022). Locally, calcite-rich shear zones are observed, showing thick homogeneous calcite-rich layers close to layers clearly resembling sheared calcite-bearing breccias (Fig. 4d). A set of shallowly NW-dipping quartz + feldspar veins and non-mineralized joints also occur (Figs. 2e, 4b), and commonly abut major mylonitic shear zones, with vein tips dragged into the main mylonitic foliation (Fig. 4b).

4.1.3. D_3. Strike-slip, brittle-ductile shear zones

D_3 structures include: (i) D_{3A}, strike-slip mylonitic shear zones reactivating pre-existent D_1-D_2 structures; (ii) D_{3B}, a set of conjugate, brittle-ductile strike-slip faults; (iii) D_{3C}, a set of

conjugate, normal dip-slip faults. D_1-D_2 structures are reactivated under brittle-ductile conditions with a dominant strike-slip kinematics (Fig. 4e-h), as inferred from the development of a sub-horizontal L_{3A} lineation overprinting the pre-existing dip-slip L_2 (Fig. 4e). The orientation of D_{3A} structures reflects the pre-existent ENE-WSW mylonitic shear zones (Fig. 2f). A heterogeneous S-C fabric is developed in major mylonitic zones, showing dominant dextral kinematics (Fig. 4e-f, same outcrop of the shear zone a few meters far from Fig. 4a). Tensile wing cracks (Figs. 4g, 2f), brecciated dilational jogs (Fig. 4h), and quartz + feldspar veins develop at high angle to D_1-D_2 shear fractures and mylonites during re-shearing under strike-slip orientations. These veins and dilational breccias can be distinguished from previous D_1 quartz-veins and breccias based on their orientation and their content of coarse quartz clear crystals.

The D_{3B} structures consist of brittle-ductile discrete faults and mylonites, arranged in conjugate sets (Fig. 5a). N-S-striking set of sinistral, strike-slip fault planes is conjugated to a WNW-ESE-striking set of dextral strike-slip fault planes (Fig. 2g). In both cases, the L_{3B} lineation is oblique (Fig. 2g), shallowly plunging toward ENE or WNW, respectively. The conjugate fault sets crop out in low-strain domains bounded by major D_{3A} shear zones. A very localized mylonitic foliation is observed along the discrete fault planes. The conjugate set of brittle-ductile faults is associated with subvertical, NW-SE-striking tensional Qz + Chl + Wm + Py + Hem veins (Fig. 5a). Such mineralization and veins are observed also in extensional jogs between overlapping en-echelon fault segments (Fig. 5a). Episyenites (i.e., quartz-depleted, vuggy altered granites) are observed close to mineralized veins and shearing planes (Pennacchioni et al., 2016).

D_{3C} structures consist of NW-SE striking faults with a dip-slip, Qz + Wm-bearing L_{3C} lineation with normal kinematics (Figs. 5b, 2h). They occur as discrete shear planes, with a near-constant spacing on the m-scale (Fig. 5b). They crop out mainly in the southern part of the RG, and they are less developed elsewhere. The dominant set of shear planes dips NE, with a pure dip-slip L_{3C} lineation. Conjugate, SW-dipping shear planes with normal kinematics also occur. In some cases, the shear plane is also characterized by a weak ductile foliation in the host rock. D_{3C} shows mutual crosscutting relationships with D_{3B} structures.

4.1.4. D_4 Zeolite- and gouge-bearing brittle faults

The latest set of deformation structures D_4 includes zeolite- and gouge-bearing brittle faults (Fig. 5c-d). They form gullies and valleys in the topography of the RG, and thus their exposure is very limited and, when present, badly preserved. When observed, the L_4 lineation is subhorizontal, consistent with a dominant dextral kinematics inferred from the few planes showing offset markers (Fig. 2i). Zeolite-bearing, fine-grained breccias are observed on anastomosing planes exploiting pre-existent D_1 shear fractures. Gouge-bearing fault zones are observed to develop at the contact between major quartzo-feldspathic mylonites and the undeformed granite (Fig. 5c-d). D_4 structures exploit pre-existent structural discontinuities, and the structural data in Fig. 2i show that D_4 structures actually reactivate and exploit the entire set of pre-existent structures.

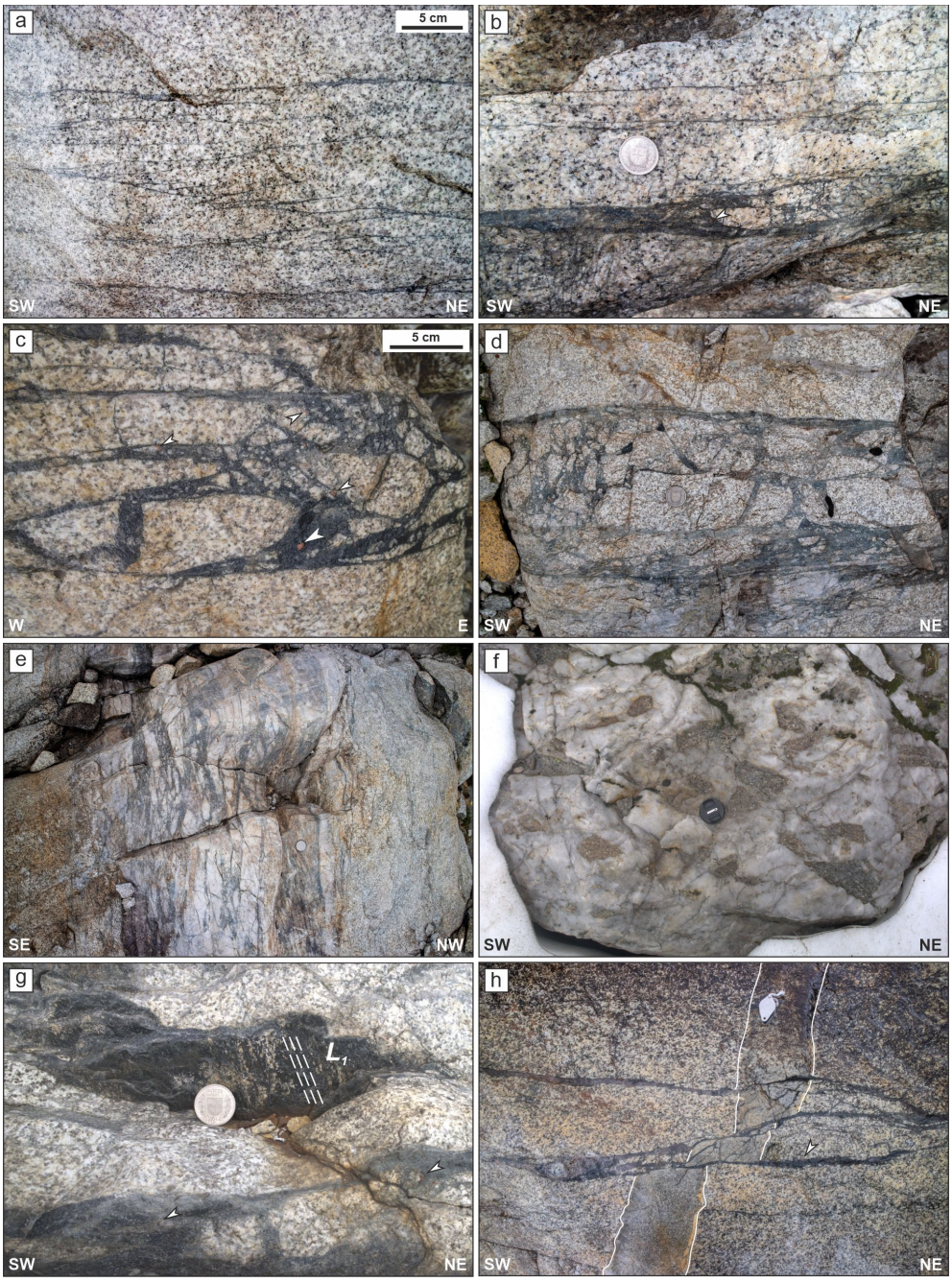

Figure 3. D_1 structures. Note that D_1 brittle structures contain clast and lithons only of undeformed granite. White arrow points to garnet in the matrix. (a) Set of quartz-biotite-bearing shear fractures showing en-echelon spatial arrangement (Wp004). (b) A cataclasite, showing limited ductile reactivation and preserving angular clasts of undeformed granite (Wp078). (c-d) Example of breccias (outcrop of sample ACB35; Wp149). (e) Sheared breccia showing moderate ductile reactivation and sheared clasts (resulting from the reworking of a thick quartz vein (Wp149). (f) Thick, plane-parallel quartz vein preserving breccia structures and undeformed granite clasts (Wp051). (g) Example of lineated surfaces in the breccia matrix (Wp149). (h)

371 Cataclasites displacing with dextral (and normal) strike-slip kinematics a subvertical pegmatitic-
372 aplitic dyke. Handlens (3 cm) for scale.

373

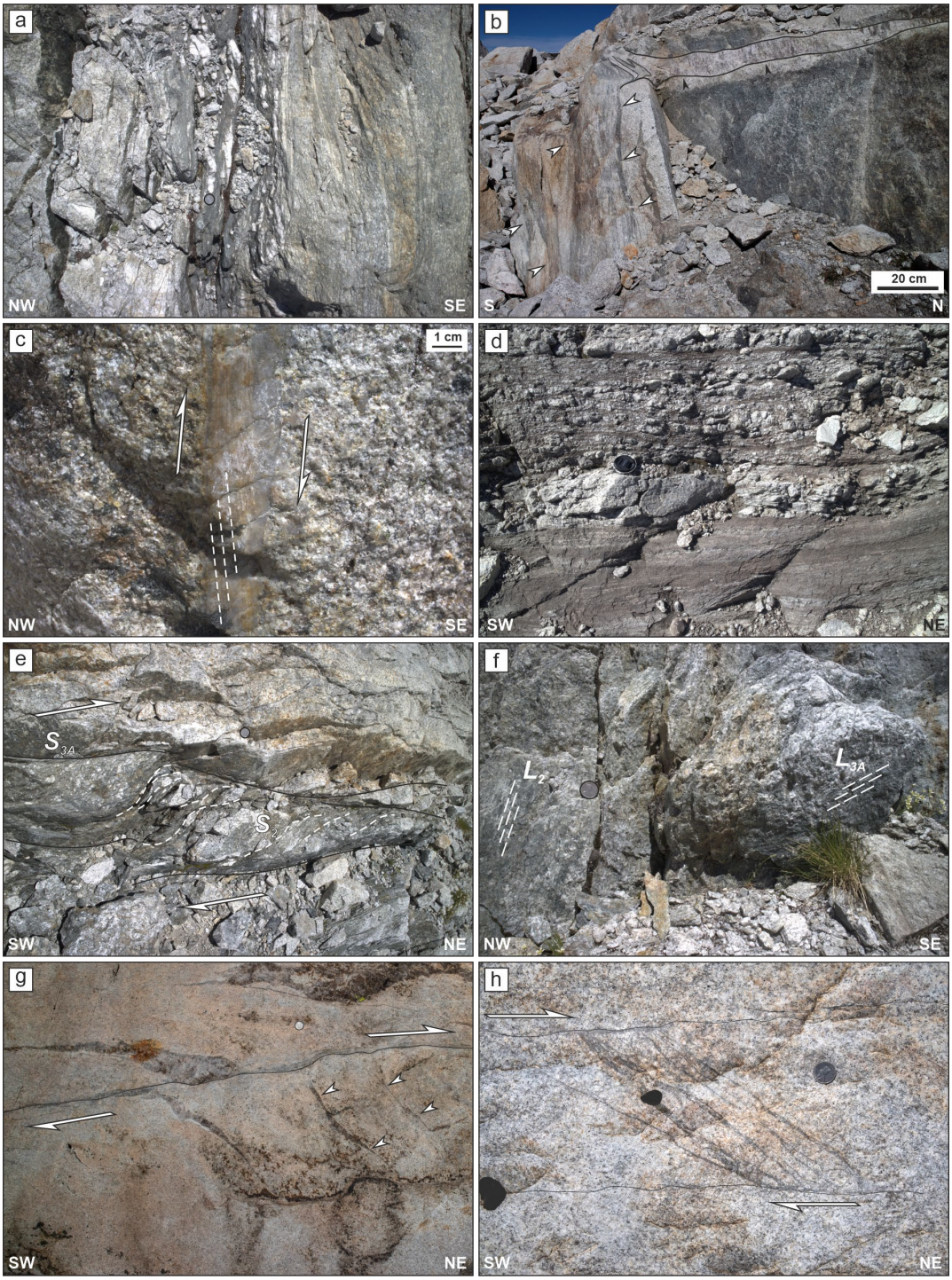

374

375 **Figure 4**. D_2-D_3 structures. (a) Dip-slip D_2 shear zone localized on a mafic dyke, parallel
376 to a set of D_1 shear fractures (left hand side of the image) and characterized by the pervasive

occurrence of sheared quartz + calcite veins. (Wp170). (b) Heterogeneous D_2 ductile shear zone (foliation marked by white arrows) with reverse kinematics and the associated low-angle Qz-vein (black arrows) (Wp087). (c) Sheared D_2 quartz + feldspar vein showing homogeneous internal foliation, suggesting top-to-SE reverse kinematics (Wp020). (d) D_2 calcite-bearing mylonite showing the boundary between a homogeneous calcite-mylonite (bottom) and a sheared breccia (top) with granitoid clasts (Wp182). (e) D_{3A} mylonitic shear zone showing S-C fabric related to strike-slip reactivation of a former dip-slip D_2 ductile shear zone (Wp171). (f) Detail of the D_{3A} shear zone reported in (e) showing the occurrence of the L_{3A}, strike-slip lineation and the L_2-dip-slip lineation on adjacent shear planes; L_{3A} lineation occurs on S-C planes of the mylonitic shear zone wrapping around lensoid domains where L_2 is still preserved. (g) D_{3A} shear fractures, showing the development of quartz + feldspar wing cracks suggesting dextral strike-slip reactivation (Wp178). (h) D_{3A} brecciated dilational jog between two reactivated D_1 shear fractures (Wp137).

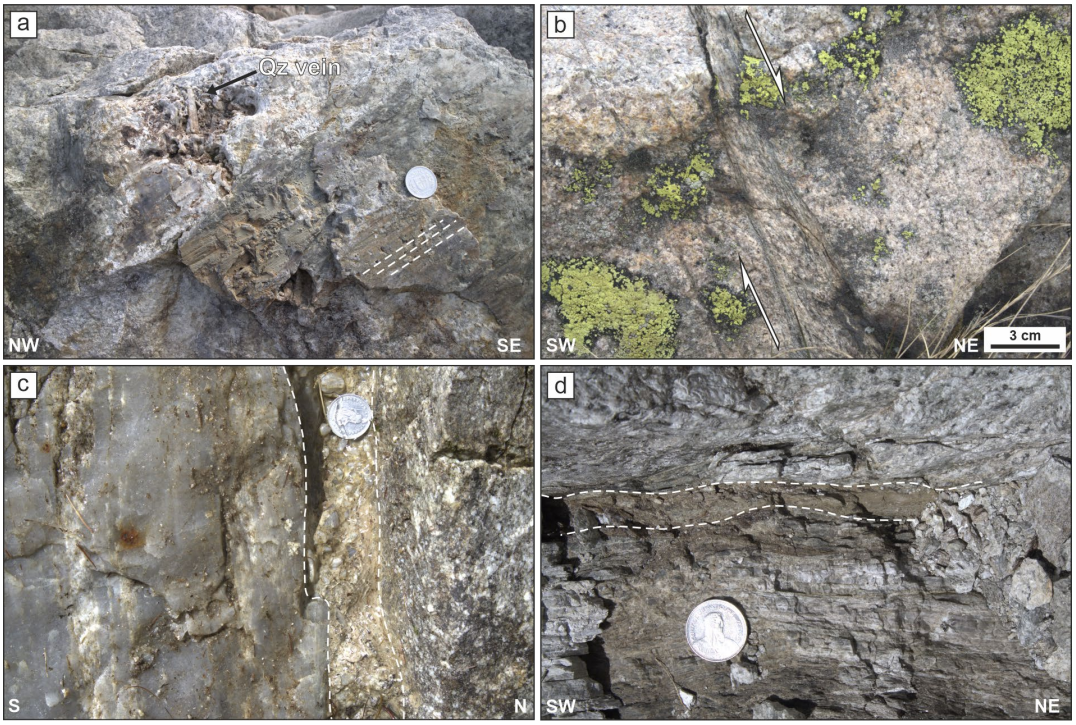

Figure 5. D_3-D_4 structures. (a) D_{3B} shear plane of a sinistral brittle-ductile fault, showing the oblique L_{3B} lineation and the occurrence of mineralized jogs (quartz vein) (Wp092). (b) D_{3C} brittle-ductile normal fault characterized by cm-scale heterogeneous foliation along the shear plane. (c) D_4 zeolite-bearing cataclasite (delimited by dashed white curves) localized at the contact between a major quartzo-feldspathic D_2 mylonite (left-hand side of the picture) and the undeformed granite (right-hand side of the picture, Wp047). (d) D_4 gouge-bearing fault localized on D_2 mylonitic foliation (Wp158).

4.2 Microstructures & petrochronology

We report here the results of microstructural, chemical and petrochronological characterization of representative samples from three of the four classes of deformation structures, including: (i) ACB35, D_1 brittle breccia (Fig. 3d-e); (ii) ACB27a, major dip-slip D_2 ductile shear zone with tip-to-SE kinematics; (iii) ACB37b, D_{3A} brittle-ductile shear zones with dextral strike-slip reactivation (Fig. 4f). Microstructure and petrography are presented together with the mineral composition obtained from EPMA. Representative mineral compositions, diagrams, and bulk rock chemical compositions are reported in the SI Tables S2-S3, and in SI Fig. S3.

4.2.1. Microstructures, mineral paragenesis and pseudosection calculations

4.2.1.1. D_1 Qz-Bt-bearing breccia

D1 breccias are composed of cm-size angular granite clasts, weakly flattened and sheared, embedded in a fine-grained matrix showing homogeneous grain size and a weak pervasive foliation defined by Bt (Fig. 6b). The matrix mineral paragenesis in ACB35 includes Qz + Bt (Mg# = 0.40-0.45; Ti = 0.02 apfu) + Kfs + Grt + Ep/Aln + Ab ± Pl ± Wm ± Chl + Ap + Zrc + Nb-Y-REE oxides and silicates (Gadolinite group). Rare Mnz grains are observed scattered in the recrystallized matrix. Grt crystals range from 100 μm to 5-10 mm, showing a wide range of crystal morphologies, from euhedral grains containing angular inclusions (Fig. 6a), to grains showing anhedral shapes, resorbed rims, and poikiloblastic/honeycomb textures (Fig 6b). In most samples of pristine D_1 breccia, euhedral Grt includes a random pattern of Qz + Pl + Kfs angular inclusions with no shape preferred orientation (Fig. 6a). These inclusions are only preserved within euhedral garnets and are here interpreted to reflect the fine-grained cataclastic matrix of the D_1 breccia on which Grt grew. There is no evidence of Grt growth and shearing coeval with D_1 brecciation. Grt grains containing angular inclusions are typically enveloped by a weak mylonitic foliation overprinting the breccia matrix (Fig. 6a-b). In some cases, Grt is weakly pleochroic, suggesting a non-cubic crystal symmetry (e.g., Cesare et al., 2019). The Grt in sample ACB35 shows an elongated shape, parallel to the foliation, with an honeycomb texture, characterized by a heterogeneous distribution of oriented inclusions (Fig. 6b). The inclusions are mainly euhedral Ep and Aln with a peculiar texture (Fig. 6c-d). Aln is observed at the core, surrounded by Ep forming the euhedral rim (Fig. 6d). Ep in the recrystallized breccia matrix shows a concentric, rhythmic zoning with brighter rims, without Aln cores (Fig. 6e-f). Ep aggregates in the recrystallized matrix contain spongy Zrc crystals, and partially destabilized Thorite-Xenotime at their core (Fig. 6f).

Grt compositional variability in this structural domain ranges from $Alm_{36}Sps_{30}Grs_{32}Prp_2$ (Grt_A) to $Alm_{36}Sps_{26}Grs_{36}Prp_2$ (Grt_B), describing a smooth gradient from the inclusion-free layer (Grt_A in Fig. 6c) toward the outer, inclusion-rich rims with honeycomb microstructure (Grt_B in Fig. 6c).

Garnets with similar compositions are also observed in sheared D_1 shear fractures and veins (samples ACB_Sp3d and ACB18, $Alm_{34\text{-}41}Sps_{26\text{-}18}Grs_{38\text{-}39}Prp_1$; Fig. 6b; SI Fig. S2a). Grt in ACB35 shows resorbed rims and embayment at the contact with the sheared granular matrix and phyllosilicates, indicating that Grt is likely metastable in the sheared mineral paragenesis (Fig. 6b-d).

The pseudosection for sample ACB35 was computed with an H_2O amount equal to the LOI content retrieved from XRF analyses (SI Table S2; Fig. 7a). The bulk composition adopted for the calculation reflects the recrystallized matrix of the breccia. Its composition is highly enriched in SiO_2 compared to the undeformed granite (SI Table S3). The observed paragenesis Qz + Bt + Kfs + Grt + Ep + Ab is computed to be stable over a wide range of *P-T* conditions (T < ~550 ºC, P < 0.9 GPa). The variation of computed Bt composition is limited and not useful to further constrain P-T conditions of apparent equilibrium. The observed Grt_A and Grt_B compositions are computed to be stable at T = 590 ± 10 ºC, and P = 0.94 GPa for Grt_A, P = 1.02 GPa for Grt_B. However, under those conditions, Ep and Ab are not stable. This misfit between observed and computed paragenesis suggests that the observed paragenesis might be metastable, preserving a porphyroclastic Grt in a recrystallized and equilibrated fine-grained matrix. In any case, similar *P-T* estimates are retrieved from pseudosection calculations using samples ACB18 (590 ± 25 ºC, 1.0 ± 0.1 GPa), as well as ACB25 (575 ± 15 ºC, 0.9 ± 0.1 GPa), the latter representing the seared contact between granite and the host rock (SI Text S2-S3).

4.2.1.2. D_2 Dip-slip, reverse shear zones

The sample ACB27a represents a high-strain domain of a D_2 ductile shear zone. D_2 ductile shear zones are characterized by a pervasive and homogeneous mylonitic foliation including Qz + Kfs + Wm (Si = 6.6-6.8) + Ep/Aln + Bt (Mg# = 0.55; Ti = 0.04 apfu) + Ab ± Pl enveloping mm-sized Wm + Bt porphyroblasts (Fig. 6g). The pseudosection was computed adopting an H_2O amount as obtained from the LOI content retrieved from XRF analyses (Fig. 8a). The observed paragenesis Qz + Bt + Wm + Kfs + Ep + Ab is computed to be stable over a wide range of *P-T* conditions, at H_2O-saturated conditions. Computed Wm(Si) is comparable to the observed composition. Considering the observed Wm(Si), Bt(Ti) = 0.03 and Bt(Mg#) > 0.5, the stability field of the observed paragenesis is constrained to T = 520 ± 40 ºC ºC and P = 0.83 ± 1.25 GPa.

4.2.1.3. D_3 Strike-slip, dextral shear zones

The ACB37b mineral paragenesis includes Qz + Kfs + Wm + Bt (Mg# = 0.58; Ti = 0.05 apfu) + Pl + Ab + Ep/Aln + Ap ± Chl (Fig. 6h). The main foliation is defined by anastomosing S-C shear planes of fine-grained Wm, incorporating Bt and Ep/Aln inclusions, wrapping around recrystallized Qz + Pl + Ab + Kfs lenses. Wm(Si) is rather variable, forming two main compositional groups which have no microstructural correspondence: $Wm(Si)_1$= 6.40 apfu and $Wm(Si)_2$ = 6.65-6.85 (SI Fig. S3a-b). The pseudosection has been computed at H_2O-saturated conditions (Fig. 8b). The observed paragenesis is stable over a wide range of *P-T* conditions. Computed $Wm(Si)_1$, and Bt(Ti) isopleths define a field centered at T = 395 ± 25 ºC ºC and P = 0.4 ± 0.1 GPa. The variability of the computed Bt(Mg#) is rather limited (0.52-0.55) and slightly underestimates the observed composition. Spn is predicted in very small amounts (>1 vol%) but not observed.

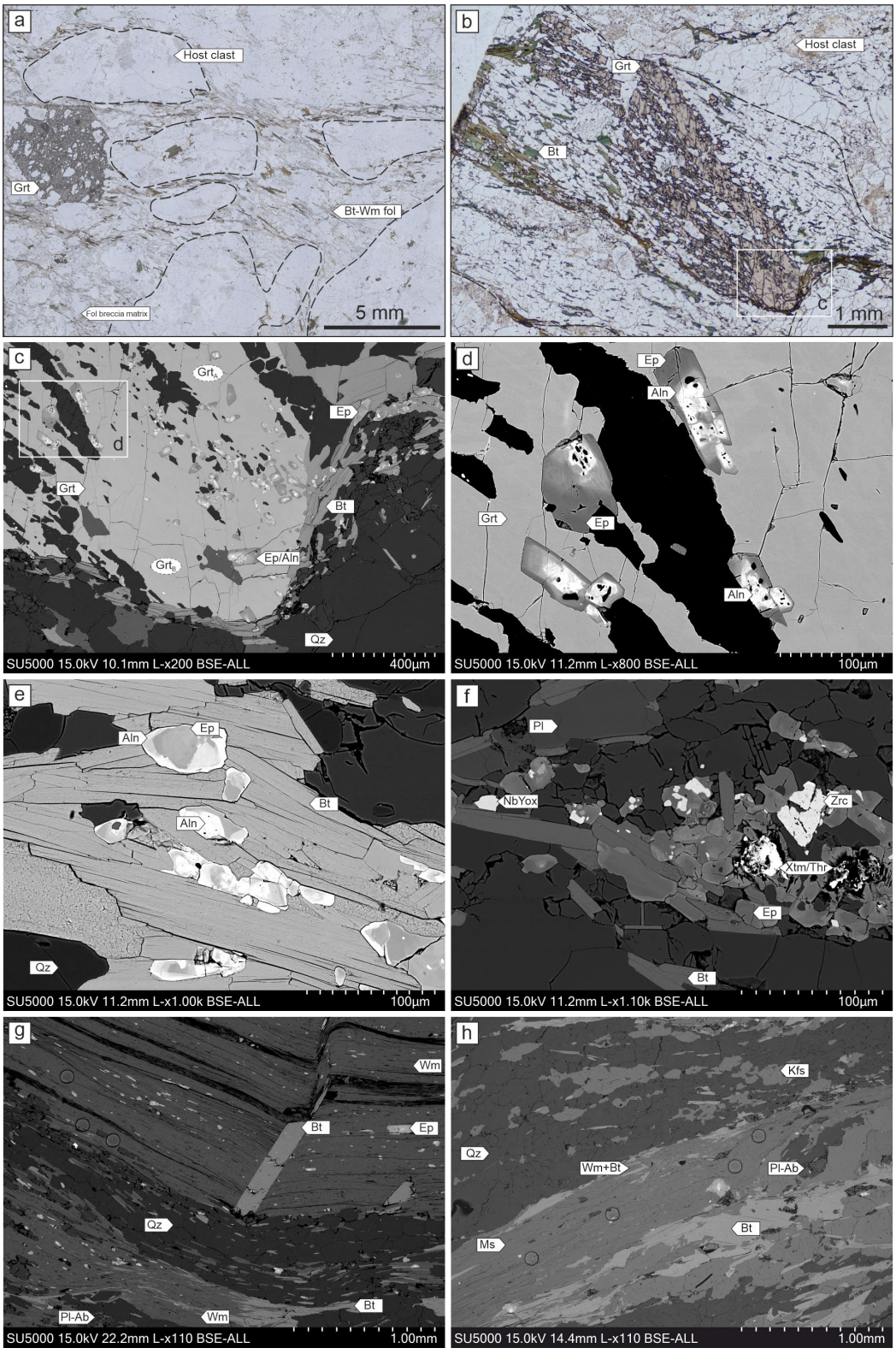

Figure 6. Microstructures of the analyzed deformation zones. (a) Optical plane-polarized light micrograph of D_1 breccias. Note the occurrence of the random pattern of inclusions in Grt formed by angular clasts. Dashed curves delimit mm-to-cm clasts of the host granite. (b) Optical

plane-polarized light micrograph of the recrystallized matrix of a D_1 breccia (sample ACB35), showing the analyzed honeycomb Grt. (c) BSE image of Grt in sample ACB35 showing the alignment of Ep/Aln inclusions. See text for explanations. (d) BSE image of the Ep/Aln inclusions in the Grt of sample ACB35, showing the Aln, inclusion-rich cores with resorption textures and euhedral Ep rims. (e) BSE image of Ep crystals included in Bt in the fine-grained matrix of sample ACB35, showing rhythmic zoning between Ep-rich and Aln-rich layers. (f) BSE image of Ep aggregates along the mylonitic foliation in sample ACB35, including Zircon (Zrc), Nb-Y-oxides (NbYox), and Xtm/Thr aggregates likely resulting from the destabilization of Monazite. (g) BSE image of sample ACB27a showing the Wm porphyroblast and mylonitic foliation. Note the craters due to laser ablation analyses. (h) BSE image of the mylonitic foliation of sample ACB37b showing the occurrence of fine-grained aggregates of Wm + Bt. Note the craters due to laser ablation analyses.

4.2.2. In-situ U-Pb on Garnet

We report here the results of U-Pb and trace element analyses from a set of samples representing D_1 breccias (ACB35; ACB_Sp8; ACB_Sp7), and sheared Qz-veins and fractures (ACB18, ACB_Sp3) (Fig. 6; SI Fig. S2).

The analyses of Grt in ACB35 show two distinct populations, defining two separate trends in a Tera-Wasserburg concordia diagram (Fig. 7b). A first population of U-Pb data forms a linear array defining a lower intercept age of 128.0 ± 9.3 Ma (n=26, MSWD=2.9). A second population can be fitted by a regression line with a lower intercept corresponding to an age of 34.0 ± 4.4 Ma (n=25, MSWD=2.8). The combination of U-Pb ratios and trace element concentrations reveals that the first population contains elevated Zr amounts (up to 7000 ppm), which are indicative of contamination of the analysis by ablation of zircon inclusions in the garnet. As shown in the trace element maps of Fig. 7c, some of the ablation spots fall adjacent to or on top of Grt areas where high amounts of Zr are detected. Therefore, to avoid contamination artifacts, we have excluded from the final age calculation all the U-Pb data with Zr content>20-30 ppm (depending on the sample). This approach filters out the anomalously old, spurious U-Pb intercept age (~128 Ma) defined above.

The pooled lower intercept Tera-Wasserburg age obtained from analyses of several small (inclusion-free) Grt grains for this (ACB35) and the other samples are reported in Table 1. Other samples range between 26.9 ± 1.3 Ma (n=54, MSWD=1.9) for ACB_Sp3b (Fig. 7e), and 20.1 ± 1.0 Ma (n=33, MSWD=0.86) for ACB_Sp8d (Fig. 7f). Additional details of U-Pb analyses, including Tera-Wasserburg plots, are reported in the SI Text S2 and Fig. S2.

The REE patterns of analyzed garnets (Fig. 7d) are characterized by a high variability in REE contents, ranging between two end members (Grt-Type1 and Grt-Type2 in Fig. 7d inset). Grt-Type1 is characterized by significant depletion of LREE with a negative anomaly of Ce, and a steep HREE slope. Grt-Type2 is characterized by a rather flat LREE-HREE profile, along with a low Sm/La (Fig. 7d). In addition, the ablation maps reveal a weak trace element zoning in Grt (Fig. 7c). A similar variation in LREE content is also observed in samples ACB18, ACB_Sp3b, ACB_Sp8c/d, ACB_Sp7d (Fig. 7d).

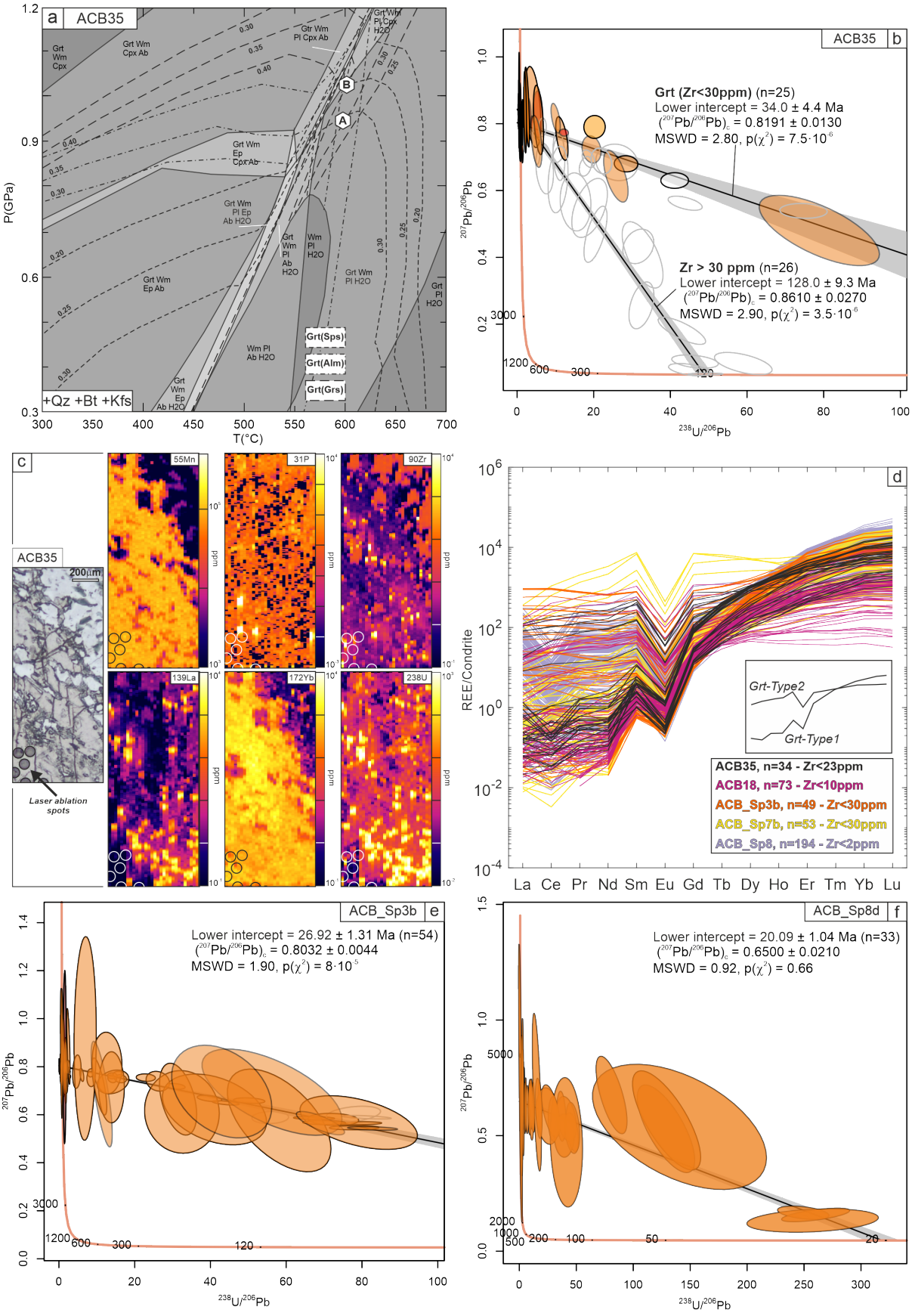
a
ACB35
P(GPa)
T(°C)
+Qz +Bt +Kfs
Grt(Sps)
Grt(Alm)
Grt(Grs)
b
ACB35
Grt (Zr<30ppm) (n=25)
Lower intercept = 34.0 ± 4.4 Ma
(207Pb/206Pb)c = 0.8191 ± 0.0130
MSWD = 2.80, p(χ2) = 7.5·10-6
Zr > 30 ppm (n=26)
Lower intercept = 128.0 ± 9.3 Ma
(207Pb/206Pb)c = 0.8610 ± 0.0270
MSWD = 2.90, p(χ2) = 3.5·10-6
207Pb/206Pb
238U/206Pb
c
ACB35
200µm
Laser ablation spots
55Mn
31P
90Zr
139La
172Yb
238U
ppm
d
REE/Condrite
Grt-Type2
Grt-Type1
ACB35, n=34 - Zr<23ppm
ACB18, n=73 - Zr<10ppm
ACB_Sp3b, n=49 - Zr<30ppm
ACB_Sp7b, n=53 - Zr<30ppm
ACB_Sp8, n=194 - Zr<2ppm
La Ce Pr Nd Sm Eu Gd Tb Dy Ho Er Tm Yb Lu
e
ACB_Sp3b
Lower intercept = 26.92 ± 1.31 Ma (n=54)
(207Pb/206Pb)c = 0.8032 ± 0.0044
MSWD = 1.90, p(χ2) = 8·10-5
f
ACB_Sp8d
Lower intercept = 20.09 ± 1.04 Ma (n=33)
(207Pb/206Pb)c = 0.6500 ± 0.0210
MSWD = 0.92, p(χ2) = 0.66

Figure 7. *P-T-t* data for sample of D1 structures. (a) Computed pseudosections for sample ACB35; (b) Tera-Wasserburg (TW) diagram of U-Pb garnet and trace element data for samples ACB35, showing the two populations of data, with analyses plotted according to their Zr content. (c) Laser ablation maps for selected isotopic masses, including ^{55}Mn, ^{31}P, ^{90}Zr, ^{139}La, ^{172}Yb, ^{238}U, on ACB35 Grt (see area delimited in Fig. 6b). (d) Chondrite-normalized (McDonough and Sun, 1995) REE-patterns of the analyzed Grt in samples ACB35, ACB18, ACB_Sp3b, ACB_Sp7c, ACB_Sp8c/d; the inset shows the compositions of the two identified end-members (Grt-Type1, Grt-Type2) characterized by either flat LREE or steep LREE profile. (e -f) TW diagram for Grt in ACB_Sp3b and ACB_Sp8d, respectively.

4.2.3. In-situ Rb-Sr on white mica and biotite

We report here the results of in-situ Rb-Sr analyses of white mica defining the main foliation in the samples ACB27a, ACB37b, already described before, as well as in an additional sample ACB12b. Then, Rb-Sr data for biotite in the undeformed granite B19-1417 are presented.

4.2.3.1. D_2 Dip-slip, reverse shear zone

In ACB27A the mica grains show a large spread in ^{87}Rb/^{86}Sr from 119 to 3125 with corresponding variations in ^{87}Sr/^{86}Sr between 0.82 and 1.42 (n = 39). A regression through these data generates an isochron with a slope corresponding to an age of 18.1 ± 0.9 Ma (2se, n = 38/39, MSWD = 1.5) and a ^{87}Sr/^{86}Sr intercept of 0.799 ± 0.010 (Fig. 7e).

4.2.3.2. D_3 Strike-slip, dextral shear zone

The analyses of mica in sample ACB37B provide different age results. Most of the analyzed grains cluster at ^{87}Rb/^{86}Sr between 700-1000 with four measurements extending to higher ^{87}Rb/^{86}Sr (up to 3030) and one to lower ^{87}Rb/^{86}Sr (4.1). ^{87}Sr/^{86}Sr values are similarly clustered between 0.86 and 0.99 with three higher (up to 1.44) and one lower value (0.77). The corresponding Rb-Sr isochron provides an age of 14.7 ± 1.5 Ma and an initial ^{87}Sr/^{86}Sr of 0.767 ± 0.018 (n = 35, MSWD = 1.3; Fig. 7f). These values change marginally if the high Sr analysis, for which contribution by a Sr-bearing phase is likely, is removed (e.g., 13.1 ± 2.1 Ma).

4.2.3.3. D_2 bulk foliation in RG_2 granite

Sample ACB12b represents the foliated RG_2 granite, where the Wm-bearing bulk foliation wraps around the porphyric Kfs and the partially recrystallized quartz domains. The recrystallized matrix along the foliation is mainly composed of Qz + Wm + Ab + Ep. White mica shows limited ^{87}Rb/^{86}Sr spread (≤352) including two relatively low values of 8.0 due to ablation of Sr-rich impurities. ^{87}Sr/^{86}Sr is also limited compared to the previous samples (≤0.83) with ^{87}Sr/^{86}Sr of 0.73 for the two low-Rb/Sr samples. The age of the Rb-Sr isochron (18.6 ± 1.9 Ma; n = 35; MSWD = 0.76; ^{87}Sr/^{86}Sri = 0.729 ± 0.005) is largely constrained by the two low Rb/Sr analyses. Exclusion of these two analyses returns a similar although much less precise of 16.3 ± 3.7 Ma. For all these samples (ACB27a, ACB37b and ACB12b) we prefer to consider the more precise isochron ages that include the high-Sr analyses because the high Sr impurities included in these analyses appear to be sourced from minerals (epidote) cogenetic with mica.

4.2.3.4. Undeformed RG_1 granite

Sample B19-1417 represents the undeformed RG_1 granite. Biotite in this undeformed granite provides similar ages to those of white mica in sheared sample ACB37B. This biotite shows very high and highly variable $^{87}Rb/^{86}Sr$ (2350-45720) corresponding to elevated $^{87}Sr/^{86}Sr$ between 1.22 and 10.5. The large spread in Rb-Sr data point results in a relatively precise isochron corresponding to an age of 15.2 ± 0.7 Ma (n = 28/30; MSWD = 0.34) but a poorly defined $^{87}Sr/^{86}Sr$ intercept of 0.68 ± 0.11 (Fig. 8f).

Biotite in RG_1 (sample B19-1417), foliated RG_2 (sample ACB14c, SI Text S4, Fig. S4) and D_2 localized shear zone in RG_2 (sample ACB3b, SI Text S4, Fig. S4) yielded indistinguishable ages (Table 1) which are all within uncertainty of the Rb-Sr age of white mica from the D_{3A} localized shear zone (Fig. 8d).

Sample	Description	Lower Intercept Age (Ma)	Uncert. Int. (±2σ, Ma)	Uncert. With Ssys (±2σ, Ma)*	Relative Uncertainty (±2σ, %)	Number of analyses	MSWD	p(χ2)
ACB18	U-Pb Grt	23.23	3.58	3.60	15.48%	45 /55	3.40	0.0
ACB35	U-Pb Grt, Zr > 25 ppm	127.97	9.08	9.28	7.25%	26 /36	2.90	0.0
	U-Pb Grt, Zr < 25 ppm	34.04	4.37	4.40	12.93%	25 /35	2.80	0.0
ACB_Sp3b	U-Pb Grt	26.92	1.25	1.31	4.88%	54 /59	1.90	0.0
ACB_Sp7b	U-Pb Grt	30.51	6.79	6.81	22.31%	57 /58	0.47	1.0
ACB_Sp8c	U-Pb Grt	24.04	2.07	2.10	8.74%	68 /71	0.92	0.7
ACB_Sp8d	U-Pb Grt	20.09	1	1.04	5.20%	33 /33	0.86	0.7
B19-1417	Bt, Undeformed RG1	15.15	-	0.71	4.69%	27 /29	0.34	1.0
ACB3b	Bt, D2 in RG1	15.25	-	0.88	5.77%	28 /30	0.65	0.9
ACB12b	Wm, Bulk RG2 fol	18.59	-	1.87	10.06%	35 /37	0.76	0.8
ACB14c	Bt, Bulk RG2 fol	15.01	-	1.17	7.79%	30 /30	0.42	1.0
ACB27a	Wm, D2	18.14	-	0.8	4.41%	38 /39	1.50	0.0
ACB37b	Wm, D3	14.68	-	1.55	10.56%	35 /36	1.30	0.1
ACB_Sp6	Bt, Bulk RG2 fol	14.77	-	0.74	5.01%	30 /30	0.65	0.9
*Systematic, long-term excess variance used for propagation is 1.5%								
Note. Samples in bold are discussed in the main text.								

Table 1. Summary of the results from U-Pb in garnet and Rb-Sr in mica analyses.

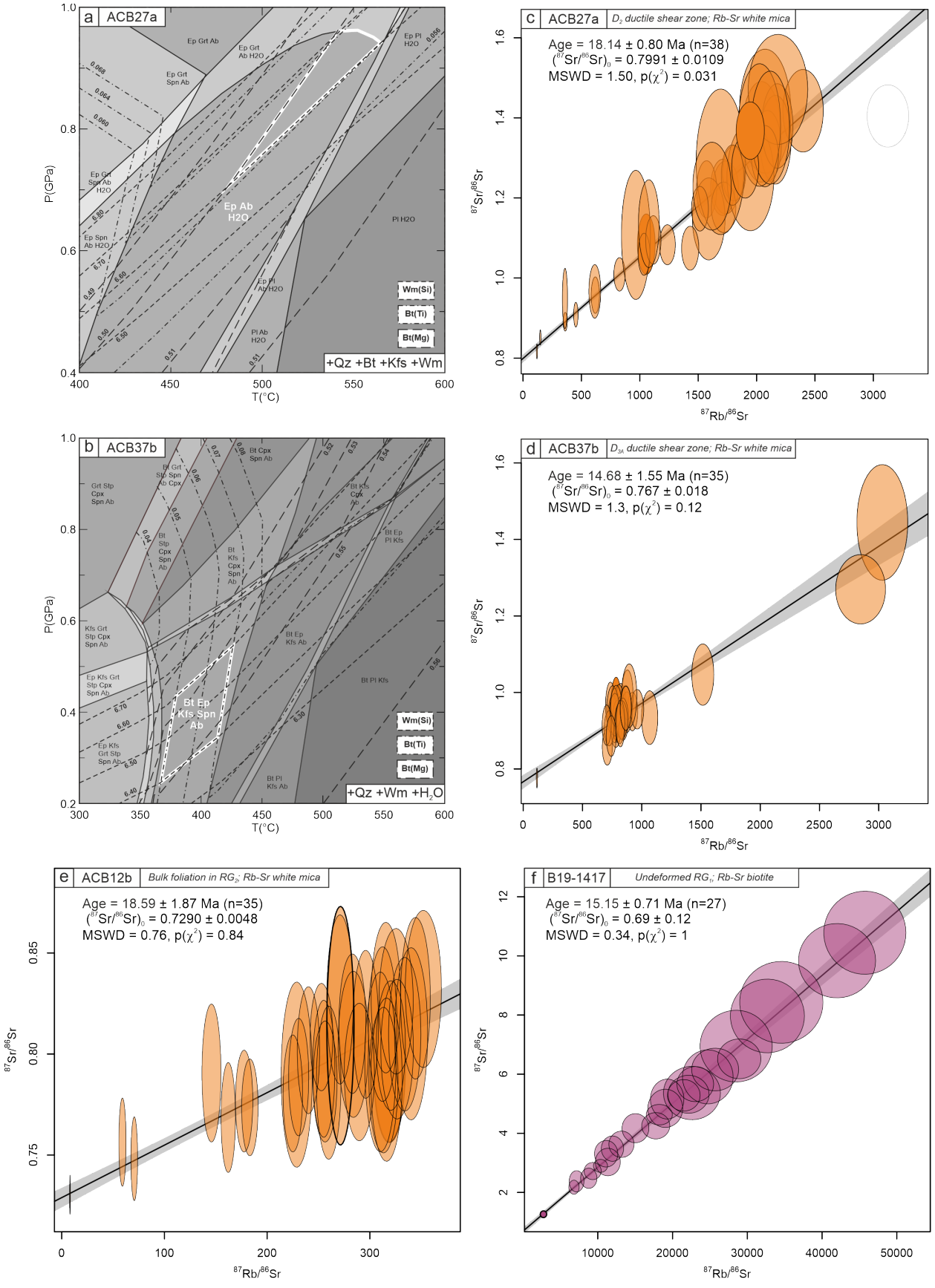
a ACB27a
Ep Grt Ab
Ep Grt Ab H2O
Ep Pl H2O
Ep Grt Spn Ab
Ep Grt Spn Ab H2O
Ep Ab H2O
Pl H2O
Ep Spn Ab H2O
Ep Pl Ab H2O
Pl Ab H2O
Wm(Si)
Bt(Ti)
Bt(Mg)
+Qz +Bt +Kfs +Wm
P(GPa)
T(°C)
c ACB27a D2 ductile shear zone; Rb-Sr white mica
Age = 18.14 ± 0.80 Ma (n=38)
(87Sr/86Sr)0 = 0.7991 ± 0.0109
MSWD = 1.50, p(χ2) = 0.031
87Sr/86Sr
87Rb/86Sr
b ACB37b
Grt Stp Cpx Spn Ab
Bt Grt Stp Spn Ab Cpx
Bt Cpx Spn Ab
Bt Stp Cpx Spn Ab
Bt Kfs Cpx Spn Ab
Bt Ep Pl Kfs
Kfs Grt Stp Cpx Spn Ab
Bt Ep Kfs Ab
Bt Pl Kfs
Ep Kfs Grt Stp Cpx Spn Ab
Bt Ep Kfs Spn Ab
Ep Kfs Grt Stp Spn Ab
Bt Pl Kfs Ab
Wm(Si)
Bt(Ti)
Bt(Mg)
+Qz +Wm +H2O
P(GPa)
T(°C)
d ACB37b D3d ductile shear zone; Rb-Sr white mica
Age = 14.68 ± 1.55 Ma (n=35)
(87Sr/86Sr)0 = 0.767 ± 0.018
MSWD = 1.3, p(χ2) = 0.12
87Sr/86Sr
87Rb/86Sr
e ACB12b Bulk foliation in RG2; Rb-Sr white mica
Age = 18.59 ± 1.87 Ma (n=35)
(87Sr/86Sr)0 = 0.7290 ± 0.0048
MSWD = 0.76, p(χ2) = 0.84
87Sr/86Sr
87Rb/86Sr
f B19-1417 Undeformed RG1; Rb-Sr biotite
Age = 15.15 ± 0.71 Ma (n=27)
(87Sr/86Sr)0 = 0.69 ± 0.12
MSWD = 0.34, p(χ2) = 1
87Sr/86Sr
87Rb/86Sr

Figure 8. *P-T-t* data for sample ACB27a-ACB37b. (a-b) Computed pseudosections for sample ACB27a and ACB37b, respectively. (c) ACB27a, (d) ACB37b, (e) ACB12b and (f) B19-1417 mica Rb-Sr isochrones including their corresponding ages (slope) and initial $^{87}Sr/^{86}Sr$ composition (intercept). The size of the ellipses indicates internal 2SE (standard error). Isochronous regressions are plotted as black lines with their 95% confidence level as gray envelopes. All plots were generated using IsoplotR (Vermeesch, 2018).

5. Discussion

Here, we discuss and interpret the field observation and petrochronological data to (1) define the time-constrained *P-T-d* path and (2) to characterize the rheological evolution of the Rotondo granite, including the factors controlling it, during collisional tectonics.

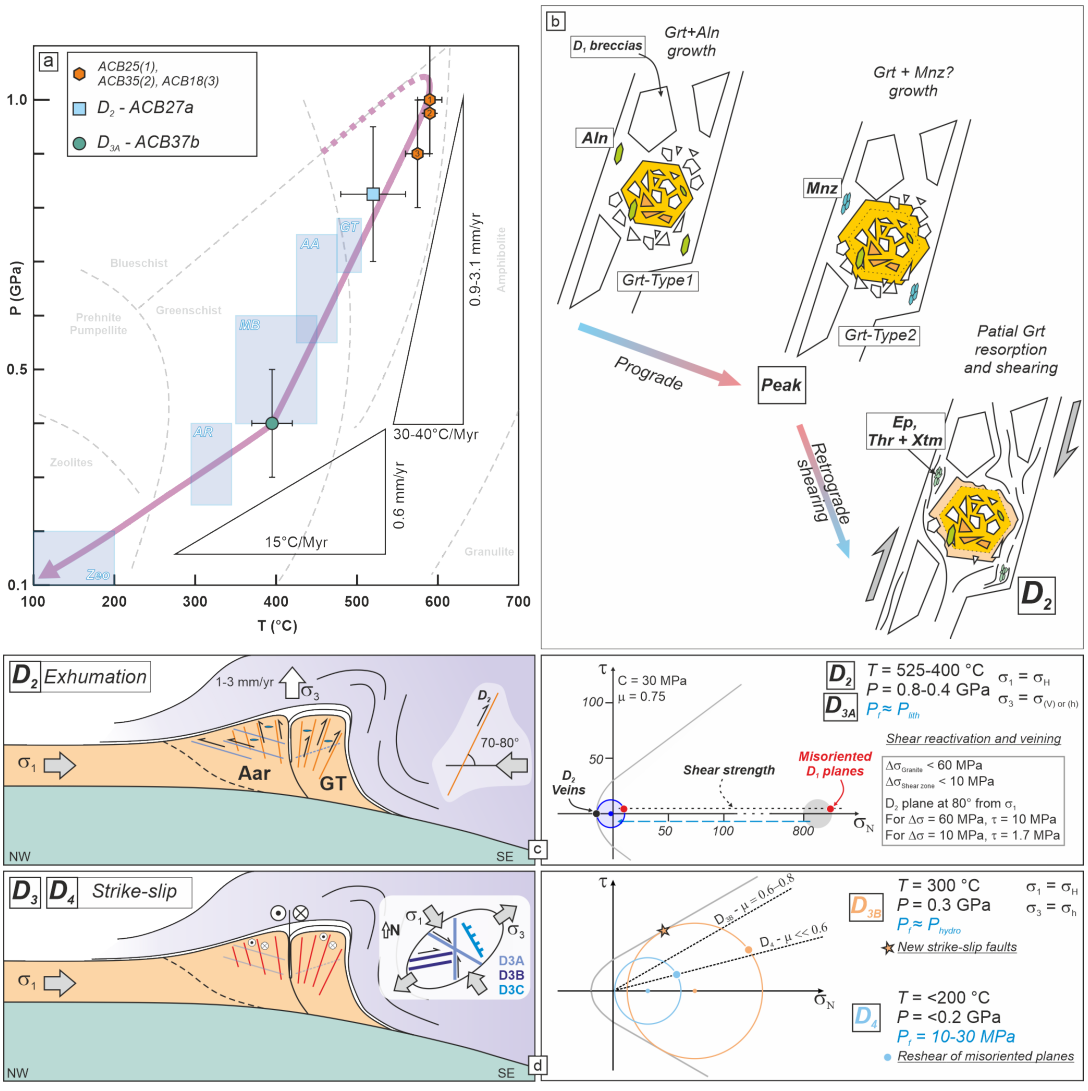

Figure 9. *P-T-t-d* path for the Rotondo granite and sketch of its tectonic evolution. (a) Diagram summarizing the *P-T* conditions of deformation retrieved from thermodynamic modeling. Light blue boxes report the *P-T* conditions of peak/retrograde shear zone from other ECMs (AA: Aar/Grimsel, Goncalves et al., 2012; AR: Aiguille Rouges, Egli et al., 2017; MB: Mont Blanc: Rolland et al., 2009; GT: Gotthard-Fibbia, Oliot et al., 2014; Zeo: zeolite-faults

593 from Lützenkirchen & Loew, 2011). Exhumation and cooling rates are reported. (b) Sketch
594 representing the possible microstructural evolution and Grt nucleation between D_1 and D_2
595 deformation stages. See text for explanation. (c-d) Sketch (not to scale) of the tectonic and
596 rheological evolution of the Rotondo granite and Gotthard nappe through the D_2-D_4 deformation
597 stages. See text for explanation. σ_V: vertical principal stress; σ_H: major horizontal stress; σ_h:
598 minor horizontal stress. Mohr plots computed with MohrPlotter
599 (https://www.rickallmendinger.net/mohrplotter). GT: Gotthard nappe; Penninic a.w.: Penninic
600 accretionary wedge.

601 5.1. P-T-t-d path and tectonic evolution

602 The *P-T-t-d* path summarizing the structural, petrochronological, and rheological
603 evolution of the granite is presented in Fig. 9.

604 5.1.1. Brittle-to-ductile evolution and Alpine peak metamorphic conditions

605 The oldest structures observed in the granite consist of D_1 shear fractures, cataclasites and
606 breccias. Similar brittle structures pre-dating ductile shear zones are reported from several other
607 crystalline units of the Alps (External and Internal Crystalline Massifs: Bertini et al., 1985;
608 Ceccato et al., 2022; Goncalves et al., 2012; Guermani & Pennacchioni, 1998; Menegon &
609 Pennacchioni, 2010; Oliot et al., 2014; Rolland et al., 2009; Wehrens et al., 2016; Tauern
610 Window: Leydier et al., 2019; Mancktelow & Pennacchioni, 2020; Suretta nappe: Goncalves et
611 al., 2016). In many cases these brittle structures were interpreted to have formed in the biotite
612 stability field, suggesting they were formed at relatively high T (>350 ºC) and mid-to-lower
613 crustal conditions (Goncalves et al., 2016; Wehrens et al., 2016). Accordingly, they have been
614 interpreted to represent either (a) a pro-grade phase of brittle Alpine deformation (Guermani &
615 Pennacchioni, 1998), or (b) brittle (seismic) deformation at mid-crustal depths at the Alpine peak
616 metamorphic conditions (Leydier et al., 2019; Mancktelow & Pennacchioni, 2020; Wehrens et
617 al., 2016). It is interesting to note that such brittle-to-ductile evolution at peak metamorphic
618 conditions has been reported from different crystalline units across the Alps spanning the whole
619 range of "peak metamorphic conditions" recorded for the different case studies, from sub-
620 greenschist to high-pressure amphibolite facies (see Ceccato et al., 2022; Fig. 9a). Conversely,
621 recent studies proposed an inherited origin for similar brittle structures occurring in the ECMs,
622 suggesting their development during the Permo-Mesozoic rifting (Ballèvre et al., 2018;
623 Dall'Asta et al., 2022; Herwegh et al., 2020).

624 Although we don't have quantitative constraints on the timing or exact *P-T* conditions of
625 formation of D_1 structures, their micro and macro-structural relationships provide several clues
626 about their relative timing with respect to Alpine collision, and their deformation conditions. In
627 terms of relative timing, firstly, a key observation is that D_1 structures are overprinted by D_2
628 mylonitic shear zones without mutual cross-cutting relationship. Secondly, in the present
629 orientation, D_1 structures are oriented at high angles (70-80º) with respect to the long-term
630 NNW-SSE shortening direction and maximum principal stress σ_1 during Alpine convergence and
631 D_2 reverse shearing (Fig. 9d-e). This high-angle orientation (much larger than the ~30º expected
632 for Andersonian thrust faults) makes it difficult to explain the origin of D_1 structures as reverse
633 brittle faults during Alpine convergence. As discussed by Herwegh et al. (2020) for similar
634 brittle structures occurring in the Aar massif, exaggerated rotation (>60º) of the entire massif
635 would be necessary to re-orient low-angle thrust planes into the observed D_1 orientation. Indeed,

such high angle orientation would be more consistent with the development of faults and fractures under a strike-slip or extensional tectonic regime (Sibson, 2003). The steep orientation of D_1 structures is a common feature of many of the shear zones presenting a brittle-to-ductile evolution in the ECMs (e.g., Bertini et al., 1985; Guermani & Pennacchioni, 1998; Oliot et al., 2014; Rolland et al., 2009; Wehrens et al., 2016; Herwegh et al., 2017, 2020). If we extrapolate our observations from the Rotondo to the other massifs, the common D_1 steep orientation suggests that little or no reorientation occurred regionally, and that this orientation might represent an original feature of the brittle deformation structures at the regional scale. These observations suggest the D_1 structures pre-date Alpine convergence, rather than being synkinematic with cyclical brittle-ductile deformation at peak metamorphic conditions, as instead proposed for other case studies (Herwegh et al., 2017; Mancktelow & Pennacchioni, 2020; Wehrens et al., 2016).

The geochemical and age relationships observed in Grt porphyroblasts that overprint D_1 structures provide further constraints on the earliest stages of Rotondo granite deformation and the transition from D_1 to D_2 structures. Firstly, Grt postdates breccia formation, statically overprinting the pre-existing texture (Fig. 6a). Later deformation during peak to D_2 retrograde shearing led to foliation development in the matrix surrounding the Grt. The foliation-parallel, elongated, and honeycomb-like crystal shapes (Fig. 6b) may suggest that Grt partially re-equilibrated or crystallized synkinematically to early D_2 shearing at conditions close to peak metamorphism. However, most of the D_2 shear zones do not contain Grt, probably indicating its metastability during the main phase of retrograde D_2 shearing related to exhumation. Thus, we define three main stages of early Rotondo evolution (Fig. 9b): (i) D_1 brecciation and cataclasis, (ii) Grt growth at a post-kinematic stage relative to D_1; (iii) shearing and likely Grt destabilization during D_2.

A diachronous two-stage evolution of Grt is supported by its REE and U-Pb systematics. The two Grt compositions (Grt-Type1, Grt-Type2), characterized by different LREE patterns have to be interpreted along with accessory mineral phases (Aln, Ep, Mnz) observed as inclusions and in the ductile matrix overprinting D_1 breccia in sample ACB35. The depletion of LREE observed for Grt-Type1 is consistent with growth of Grt in apparent equilibrium with accessory phases preferentially partitioning LREE, such as Aln. Indeed, Aln inclusions are (only) observed in some of the analyzed garnets. Similarly, the enrichment of LREE observed in Grt-Type2 is consistent with garnet growth at conditions where LREE-rich phases (e.g., Aln) are not stable anymore and the only phase capable of incorporating LREEs is garnet. In fact, Ep-rich/Aln-poor grains are observed in the paragenesis of the sheared breccia matrix, surrounding Xtm/Thr aggregates, in turn resulting from the destabilization of first generation Aln or Mnz (Fig. 6f; Janots et al., 2008; Hentschel et al., 2020). In summary, a first phase of Grt (Grt-Type1) crystallization in apparent equilibrium with Aln is followed by a second phase of crystallization of Grt (Grt-Type2) during which Aln was not stable anymore, replaced by Mnz during prograde metamorphism (e.g. Janots et al., 2008, 2009; Spear, 2010). The exact T of transition from Aln-bearing to Mnz-bearing paragenesis could shift from $T \sim 350$ ºC to $T \sim 550$ ºC depending on the bulk CaO and REE content of the rock (Spear, 2010). A similar prograde crystallization sequence has been reported from metapelites in the south-eastern Gotthard nappe described by Janots et al. (2008, 2009). In that case, prograde destabilization of Aln close to peak conditions of about 560-580 ºC formed the Mnz and REE-poor Ep aggregates observed in the recrystallized metapelite hosting the Grt (Janots et al., 2008). Mnz is rare in our samples, and it is likely that Mnz destabilization during retrograde D_2 shearing at amphibolite-to-greenschist facies

682 conditions may have led to the formation of the Ep + Xtm/Thr aggregates observed in the
683 recrystallized breccia matrix (e.g., Hentschel et al., 2020). Therefore, Ep/Aln microstructures in
684 ACB35 Grt likely record a prograde-to-peak crystallization sequence (Fig. 9b). Interestingly, in
685 both ACB35 and especially ACB18 samples, the compositional zoning of garnet suggests
686 increasing *P-T* conditions from core to rim (Fig. 7a, SI Fig. S2b).

687 U-Pb dating of Grt results in scattered ages ranging from ~34 to ~20 Ma, which is
688 broadly consistent with the ages for the regional peak metamorphism obtained from other case
689 studies in the Gotthard nappe (22-19 Ma, Janots et al., 2009; Janots & Rubatto, 2014; Boston et
690 al., 2017) and nearby Lepontine Dome (32-22 Ma, Rubatto et al., 2009). The peak metamorphic
691 conditions are constrained by pseudosections calculated for different samples (ACB35, ACB25,
692 ACB18) at 590 ± 15 ºC and 0.9 ± 0.1 GPa. The obtained *P-T* conditions are consistent with
693 recent estimates of Alpine peak metamorphic conditions from the southern Aar massif and
694 Gotthard nappe (Berger et al., 2020; Janots et al., 2008, 2009; Nibourel et al., 2021; Wiederkehr
695 et al., 2011), as well as the Penninic units of the Northern Lepontine dome (Boston et al., 2017;
696 Galli et al., 2007). The 34-20 Ma age spread would describe a prolonged thermal peak in the
697 Gotthard nappe lasting for ~10 Myrs (Fig. 9b). This conclusion is consistent with
698 geochronological data supporting the occurrence of a prolonged thermal peak starting at ~32-34
699 Ma in several other ECMs and Penninic units, lasting until 22-17 Ma when the main phase of
700 exhumation occurred (Boston et al., 2017; Cenki-Tok et al., 2014; Egli et al., 2016; Girault et al.,
701 2020; Janots et al., 2008, 2009; Rolland & Rossi, 2016; Rubatto et al., 2009; Sanchez et al.,
702 2011).

703

704 5.1.3. Exhumation – D_2 shear zones

705 The reverse kinematics of D_2 shear zones and the occurrence of associated shallowly
706 dipping tensional veins constrain a subhorizontal σ_1, parallel to a NW-SE trending maximum
707 shortening axis ε_1, and perpendicular to a subvertical σ_3 (Fig. 9c). Based on the results of
708 pseudosection calculation, these shear zones were already active at 520 ± 40 ºC and 0.82 ± 0.12
709 GPa. The conditions of re-equilibration of the analyzed samples (ACB27a T > 500 ºC) are
710 similar to the closure temperature for Rb-Sr in white mica inferred for similar case studies of
711 granitoid shear zones ($T \leq$ 500-550 ºC; e.g., Egli et al., 2015; Ribeiro et al., 2023). Therefore, it
712 is very likely that the obtained Rb-Sr date of 18.1 ± 0.8 Ma (Fig. 8) reflects the (re-)
713 crystallization of white mica in D_2 ductile shear zones. D_2 ductile shear zones accommodate the
714 main phase of tectonic exhumation of the Gotthard nappe through reverse shearing on NW-
715 steeply dipping planes. Rb-Sr dating of white mica indicates that the bulk foliation of RG_2
716 developed during the same amphibolite-facies deformation event at 18.6 ± 1.9 Ma (sample
717 ACB12b, Fig. 8e). However, biotite in D_2 shear zones (15.3 ± 0.9 Ma, sample ACB3b, SI Text
718 S4, Fig. S4) provides a younger Rb-Sr age which indicates either a later deformation event or,
719 more likely, reflects the lower closure temperature of the Rb-Sr isotope system in biotite (≤350-
720 400°C; e.g., Jenkin et al., 2001) compared to white mica (≤500°C). The exhumation of the ECMs
721 in the Central and Western Alps have been accommodated by similar steeply-dipping, reverse
722 shear zones developed during retrograde greenschist facies conditions between 22 and 17 Ma
723 (Cenki-Tok et al., 2014; Goncalves et al., 2012; Herwegh et al., 2020; Rolland et al., 2008).

724

725 5.1.4. Strike-slip tectonics – D_3-D_4

726 The kinematics and geometrical relationships of D_{3A} and D_{3B} structures constrain their
727 development under a transpressional strain field developed during NW-SE convergence (D_{3A}-
728 D_{3B}), associated with NE-SW-directed extension (D_{3B} tensional veins and D_{3C} normal faults; Fig.
729 9d). The kinematics of D_3 shear zones and tensional veins constrain a subhorizontal σ_1 and
730 maximum shortening axis ε_1 oriented ~NW-SE and a sub-horizontal, NE-SW-oriented σ_3 (Fig.
731 9d). Strike-slip D_{3A} shearing is constrained to develop at 395 ± 25 ºC and 0.4 ± 0.1 GPa. At these
732 temperature conditions, the Rb-Sr chronometer applied to white mica constraints the age of mica
733 (re-)crystallization because the closure temperature of Sr diffusion in white mica is considerably
734 higher (see previous section). Hence, the 14.7 ± 1.6 Ma age of white mica in D3A sample
735 ACB37b (Fig. 8) probably constrains the age of this deformation event. The occurrence of
736 similar Rb-Sr ages for white mica (ACB37b, D3A) and biotite (B19-1417, undeformed granite:
737 15.5 ± 0.7 Ma; ACB3b and ACB14c, foliated granite: 15.3 ± 0.9 Ma and 15.0 ± 1.2 Ma,
738 respectively; Table 1, Fig. 8, and SI Fig. S4), regardless of the intensity of sample deformation,
739 suggests that the D_{3A} deformation event occurred at conditions broadly corresponding to the
740 closure temperature of the Rb-Sr chronometer in biotite, that is ~≤350 °C (e.g., Jenkins et al.,
741 2001). If the temperatures were substantially higher (e.g., 400-500 °C), white mica would have
742 recorded an older age due to its higher closure temperature for the Rb-Sr isotope system. In other
743 words, the ~15 Ma age of biotite in the undeformed Rotondo granite represents a cooling age.
744 The overlap of white mica and biotite Rb-Sr ages implies that ductile reactivation of D_2 under
745 strike-slip conditions leading to D_{3A} shear zones occurred during a very short time period at ~15
746 Ma. Further deformation during D_3 strike-slip tectonics was accommodated by brittle-ductile
747 transpressional and extensional faults. The NW-SE-striking extensional veins associated to this
748 brittle-ductile deformation event in the Lepontine dome and Aar-Gotthard area are consistently
749 dated to <14 Ma (Bergemann et al., 2020). The contemporaneous (or cyclic) development of
750 D_{3B}-D_{3C} extensional and transpressional structures is consistent with the regional tectonic setting
751 during the activity of the Rhone-Simplon fault system (Campani et al., 2010), accommodating
752 NE-SW extensional tectonics under a constant dominant NW-SE transpression.

753 Late D_4 zeolite- and gouge-bearing brittle faults reactivated the pre-existing, steeply
754 dipping structural discontinuities under strike-slip conditions (Lützenkirchen & Loew, 2011).
755 Their activity is constrained to have occurred between 12 and 3 Ma based on K-Ar illite dating
756 (Kralik et al., 1992; Pleuger et al., 2012) at upper crustal levels (T < 200 ºC, depth <7 km;
757 Lützenkirchen & Loew, 2011). These chronological constraints are consistent with the prolonged
758 Neogene activity of the Periadriatic-Simplon-Rhone fault system (Ricchi et al., 2019).

759 In conclusion, the brittle-ductile-brittle evolution inferred from the sequence of
760 deformation structures in the Rotondo granite is the result of pre-Alpine tectonics overprinted by
761 the peak-and-retrograde collisional Alpine tectonics. Pre-collisional structures apparently
762 controlled the localization and accommodation of collisional strain in the crystalline unit.

763 5.1.5. Exhumation and cooling rates during Alpine collision

764 Rates of tectonic exhumation and cooling can be calculated considering the constraints on
765 *P*, *T*, and age of deformation provided above (Fig. 9a). Rates are computed considering a
766 geothermal gradient of 25 ºC/km and a lithostatic pressure gradient of 27.5 MPa/km (e.g.,
767 Nibourel et al., 2021). Exhumation from peak conditions at 590 ºC and 0.9 GPa at 34 to 20 Ma
768 (U-Pb of garnet) to 520 ºC and 0.8 GPa (D_2 conditions) at 18 Ma (Rb-Sr in white mica) occurred

at a rate of 0.22 to 1.8 mm/yr (km/Myr), associated with a cooling rate ranging between 5 to 35 ºC/Myr, respectively for the oldest and youngest U-Pb ages. Most of the exhumation was accommodated through the activity of D_2 ductile reverse shear zones. They accommodated the exhumation from D_2 conditions (520 ºC and 0.8 GPa) at 18 Ma (Rb-Sr on white mica) to D_3 conditions (395 ºC and 0.4 GPa) at ~14 Ma (Rb-Sr on white mica and biotite). Related exhumation rates range between 3.8 and 5.1 mm/yr, with an associated cooling rate of 30-40 ºC/Myr. On average, the exhumation from peak metamorphic conditions at 34-20 Ma to the brittle-ductile conditions recorded after D_{3A} deformation at 14 Ma occurred at an average exhumation rate of 0.9-3.0 mm/yr, associated with a cooling rate of 10-30 ºC/Myr. Such exhumation rates are comparable to those retrieved from regional thermochronometry (~1-3 mm/yr; Glotzback et al., 2010; Herwegh et al., 2020; Nibourel et al., 2021). Similarly, the high cooling rates recorded during D_2-D_3 exhumation are compatible with the estimates of 30-40 ºC/Myr provided by Janots et al. (2009) for the eastern Gotthard nappe.

After the exhumation through the brittle-ductile transition, and the switch to regional transpression, the exhumation became much slower, as constrained by comparing D_3 Rb-Sr white mica/biotite ages and the youngest K-Ar illite age (3 Ma) Kralik et al. (1992) and Pleuger et al. (2012) for gouge-bearing faults similar to D_4 structures. The obtained exhumation rate of ~0.6 mm/yr is associated with a cooling rate of ~15 ºC/Myr (Fig. 9a), similarly to what previously reported from thermochronological constraints (Glotzback et al., 2010; Herwegh et al., 2020).

5.2. Rheological evolution of the Rotondo granite during Alpine collision

In the RG, collisional shortening is accommodated through the reactivation and shearing of pre-collisional D_1 structures and pre-existing compositional and structural heterogeneities at different scales. In the current orientation D_1 brittle structures are severely misoriented, forming high angles to the maximum principal stress expected during NW-directed Alpine convergence and collision (Rosenberg et al., 2021). Despite this fact, these structures influenced the rheology and localized strain throughout the whole D_2-D_4 evolution across different *P*-*T* and rheological conditions of the crystalline basement (Fig. 9c-d). In the following sections, we constrain the rheology, as well as the stress and fluid regimes at which D_1 to D_4 structures likely formed.

The current high-angle dip of the D_1 brittle structures would be more compatible with an extensional or strike-slip tectonic regime than with a compressional/convergent setting. Given the uncertainty regarding the tectonic regime and original orientation of D_1 structures, we can only speculate about the values of differential stress ($\Delta\sigma$) and pore fluid pressure (P_f) during D_1 development. The occurrence of thin shear fractures and cataclasites may indicate a dynamic environment characterized by variable $\Delta\sigma$ ($> 4 \cdot Ts$-$5.6 \cdot Ts$, with Ts: tensile strength) and low P_f. Furthermore, the mutual overprinting between breccias and (fault-)veins implies cyclical variation of P_f and permeability in the brittle regime. Fluid-assisted brecciation is related to transient fluid-pressure increase in low-permeability rocks and facilitated in extensional regimes, as well as along pre-existing structures (Jébrak, 1997; Sibson et al., 1988). Fault-veins (lenticular Qz-veins parallel to the shear plane) suggest the fluid-driven reactivation of a pre-existing structure, at low $\Delta\sigma$ and likely sublithostatic P_f (probably < 300 MPa in the brittle field; Sibson et al., 1988). Similar conclusions can be drawn from the geometry of breccias, locally resembling crackle and mosaic breccias with randomly distributed fractures (Fig. 3c-d). These geometries

indicate very low $\Delta\sigma$ ($< 4 \cdot Ts$), and effective $\sigma 1$ close to zero ($\Delta\sigma \sim Ts$; Woodcock et al., 2007), and they are in some instances interpreted as resulting from seismic activity (Sibson, 1985, 1987; Melosh et al., 2014). Nonetheless, we cannot exclude that at least part of the veining occurred during prograde (brittle) reactivation of D_1 misoriented faults under compression, defining a general fault-valve behavior (Sibson et al., 1988). Such activity, if present, was only limited to pre-peak and brittle conditions, given the lack of brittle-over-ductile overprint in D_1 structures.

During D_2-D_3 retrograde shearing at amphibolite-to-upper greenschist facies conditions (T = 400-520 ºC, P = 0.4-0.8 GPa), the granite was characterized by a network of high strain shear zones, localized on magmatic (aplitic, mafic dykes) and tectonic (D_1) precursors, delimiting low strain domains of relatively undeformed granite. D_2 shear zones are oriented at high angle (70-80º) to the principal stress σ_1 (Fig. 9d-e). Accordingly, shearing on D_2 planes developed even if the resolved shear stress was very small, thus suggesting a limited shear strength of such D_2 ductile shear zones. Shear zone strength was controlled by reaction-weakening processes related to plagioclase destabilization, which led to the activation of fluid-mediated grain-size sensitive deformation mechanisms, as observed in similar granitoid ductile shear zones (Ceccato et al., 2022; Oliot et al., 2014). This localized weakening might have been related to the higher fluid content of D_1 structures exploited by D_2 compared to the host rock. This higher fluid content is likely related to either a fluid-bearing mineral paragenesis of former D_1 structures, or to the increased permeability of the granite along D_1 structures promoting fluid flux during retrograde D_2 shearing (e.g., Oliot et al., 2010). Further analyses would be necessary to discern between the two options and to understand the origin of the fluids and weakening. In any case, ductile shear zones acted as fluid pathways during D_2 deformation as can be inferred from the occurrence of sheared Qz + Cal veins (Fig. 4a), including Cal porphyroclasts (Fig. 11 of Rast et al., 2022). Cal porphyroclasts in Qz-mylonites have been constrained to develop during ductile shearing at low $\Delta\sigma$ (<10 MPa) at amphibolite facies, fluid-rich conditions (Mancktelow & Pennacchioni, 2010). This further suggest that the D_2 ductile shear zones were extremely weak and able to accommodate strain at very low shear stresses, probably on the order of few (1-4) MPa, considering a $\Delta\sigma$ of 10 MPa) and an orientation of 80 with respect to σ_1 (Fig. 9c). Accordingly, the pervasive occurrence of tensional veins in the undeformed granite indicates high (quasi-supralithostatic) P_f and limited $\Delta\sigma$ ($<4 \cdot Ts$, in the range 36 to 60 MPa for granite, Cox, 2010; Etheridge, 1983; Sibson, 2003; Sibson et al., 1988). Therefore, during D_2-D_3 ductile shearing: (i) there is a difference in the maximum $\Delta\sigma$ of ~25-50 MPa between weak shear zones (<10 MPa) and in the low-strain granite (<60 MPa); (ii) the strength of both high-strain shear zone and low strain granite domains is limited by tensional veining related to fluid overpressure, which in turn implies (iii) low permeability in the low strain granite during ductile deformation. D_2 ductile shear zones might have acted as higher-permeability fluid conduits, but overall the permeability was not high enough to allow the dissipation of P_f build-up to supralithostatic conditions.

During further cooling and exhumation (T < 350 ºC, P = 0.2-0.4 GPa), pre-existent misoriented structures failed to be reactivated (Fig. 9d). The development of new conjugate faults (D_{3B}) suggests increasing $\Delta\sigma$ ($>5.6 \cdot Ts$) and decreasing P_f (probably close to hydrostatic conditions) during strike-slip deformation across the brittle-ductile transition. The decreased P_f was also related to the increased porosity and permeability of the granite during this deformation stage. High permeability of such deformation structures is documented by the pervasive occurrence of mineralized open veins along fault shear planes (Fig. 5a), as well as by the

858 occurrence of high-porosity hydrothermal alteration and the development of episyenites
859 (Pennacchioni et al., 2016).

860 At shallow crustal levels ($T < 200$ ºC, $P < 0.2$ GPa), D_4 zeolite- and gouge-bearing faults
861 reactivated the rock fabrics and pre-existent structural heterogeneities instead of developing new
862 fractures and fault zones (Fig. 9d). Fluids leading to the crystallization of zeolites percolated
863 through the highly permeable network of pre-existing fractures and structural heterogeneities.
864 Similar zeolite-bearing fractures and faults are reported from the granitoid plutons of the Central
865 and Eastern Alps (e.g., Adamello: Pennacchioni et al., 2006; Rieserferner: Ceccato &
866 Pennacchioni, 2018), as well as from all the crystalline massifs of the Central Alps (e.g.,
867 Weisenberger and Bucher, 2010). For instance, in the Adamello, similarly to the Rotondo, zeolite
868 veins and gouges are observed to intrude the pre-existent fracture and fault network, locally
869 reactivating fault planes (Pennacchioni et al., 2006). The observed complex kinematics of
870 reactivation and the fluid-overpressure inferred from the occurrence of zeolite-bearing veins and
871 gouges were interpreted to be the result of earthquake swarm activity at shallow crustal levels
872 (Dempsey et al., 2014). In that case, zeolite-bearing gouges were developed during transient
873 high-stress or high pore-fluid pressure events. In the RG, low P_f of 10-30 MPa were estimated
874 from the stability of fault zeolite paragenesis (Lützenkirchen & Loew, 2011). In addition,
875 shearing planes in the granite are highly misoriented with respect to the NW-SE Alpine
876 shortening direction. Thus, transient high differential stress would have promoted the
877 development of new conjugate shear fractures, rather than reactivating misoriented planes.
878 Nonetheless, D_4 structures localize on D_1-D_2-D_3 structures (Lützenkirchen & Loew, 2011),
879 which are characterized by phyllosilicate-bearing fabrics that affect the frictional and cohesion
880 properties of the shearing planes at brittle conditions (Bistacchi et al., 2012; Volpe et al., 2022;
881 Pozzi et al., 2022). In addition, the low frictional properties of the fault gouges developed during
882 shearing might have further promoted the localization of brittle faulting on highly misoriented,
883 and otherwise frictionally-locked, fault planes during the latest stages of Alpine brittle
884 deformation (Bistacchi et al., 2012; Collettini et al., 2019; Volpe et al., 2023).

885

886 **6. Conclusions**

887 The *P-T-t-d* evolution of the Rotondo granite is recorded by a brittle-ductile-brittle
888 structural evolution. D_1 breccias and cataclasites develop in the Rotondo granite before the
889 attainment of the Alpine peak metamorphic conditions, the latter occurring between 34 and 20
890 Ma and recorded by U-Pb in garnet. Peak metamorphic conditions are closer to the amphibolite
891 facies ($T > 550$ ºC, $P > 0.7$ GPa) than those previously proposed for the ECMs and the Gotthard
892 nappe ($T < 450$-500 ºC, $P < 0.5$-0.6 GPa; Todd and Engi, 1997). Retrograde exhumation was
893 then controlled by reverse ductile shearing on D_2 ductile shear zones, localized on pre-existent
894 structural and compositional heterogeneities. The very limited shear strength of D_2 ductile shear
895 zones allowed it to accommodate fast exhumation of the Gotthard nappe at 1-3 km/Myr between
896 20 and 14 Ma. Further exhumation was accommodated at slower rates by D_3 greenschist facies
897 ($T <$400 ºC, $P < 0.4$ GPa) ductile and brittle-ductile shear zones, developed as a local response to
898 the regional strike-slip activity of the Simplon-Rhone fault system.

899 Based on the common structural and tectonometamorphic history of the Rotondo granite
900 and the other ECMs in the Central and Western Alps, we can extrapolate the results obtained

from the Rotondo to infer fundamental implications for the rheology of the European continental crust during Alpine collision:

- The European continental crust, now exposed in the ECMs, was extremely weak during Alpine continental collision and deformation at amphibolite-to-greenschist facies.
- The occurrence of inherited tectonic and primary (e.g., magmatic) fabrics and structures, although highly misoriented, clearly controlled strain geometry and localization throughout their entire rheological and metamorphic evolution.
- The main weakening event occurred during retrograde conditions.

The weakness of the European continental crust during Alpine collision allowed it to focus and localize collisional strain in the external domains of the orogen, promoting the localized and fast exhumation of the crystalline massifs ahead of the advancing dry and strong Adriatic lower crust. At the scale of the orogen, collisional shortening was therefore accommodated through the localized, and fast exhumation of the External Crystalline Massifs, by means of the activity of weak ductile shear zones, localized on pre-existing tectonic and primary fabrics.

Acknowledgments

This paper is FEAR Publication #19. This research is supported by ETH Zurich research funds to WMB and the European Research Council (ERC) Synergy project "Fault Activation and Earthquake Rupture" (FEAR) (grant 856559) granted to Domenico Giardini, Stefan Wiemer, Massimo Cocco, and Florian Amman. Markus Rast is warmly thanked for the introduction to the Bedretto tunnel geology and for providing the sample B19-1417 and thin sections adopted for Rb-Sr analysis of biotite. Neil Mancktelow and Bernardo Cesare are thanked for fruitful discussions about regional geology and garnet petrography. The authors acknowledge Luiz G. Morales and ScopeM for their support and assistance during SEM data acquisition and processing. Julien Allaz is thanked for EPMA data acquisition and technical assistance. Remy Lüchinger and Lydia Zender are gratefully acknowledged for their support during thin section preparation and XRF analyses, respectively. The crew of the Capanna Piansecco and SAC-CAS Bellinzona & Valli are warmly thanked for their logistic support, and their friendly and unconditional hospitality during fieldwork in the Rotondo area. The authors acknowledge the logistic support from the Bedretto Lab team.

Open Research

Chemical and geochronological data supporting the conclusions of the present study are reported in the main text and in the Supplementary Information files. The dataset is also available at ETH Zurich Research Collection via https://doi.org/10.3929/ethz-b-000644819 with Creative Commons Attribution 4.0 International license (Ceccato et al., 2023).

941 **References**

942 Aysal, N. et al., 2023, A New Natural Secondary Reference Material for Garnet U-Pb
943 Dating by TIMS and LA-ICP-MS. Geostandards and Geoanalytical Research, p. ggr.12493,
944 doi:10.1111/ggr.12493.

945 Ballèvre, M., Manzotti, P., & Dal Piaz, G. V. (2018). Pre-Alpine (Variscan) inheritance:
946 a key for the location of the future Valaisan basin (Western Alps). Tectonics, 37(3), 786–817.
947 https://doi.org/10.1002/2017tc004633

948 Behr, W. M., & Platt, J. P. (2014). Brittle faults are weak, yet the ductile middle crust is
949 strong: Implications for lithospheric mechanics. Geophysical Research Letters, 41(22), 8067-
950 8075. https://doi.org/10.1002/2014GL061349

951 Behr, W. M., & Platt, J. P. (2013). Rheological evolution of a Mediterranean subduction
952 complex. Journal of Structural Geology, 54, 136-155. https://doi.org/10.1016/j.jsg.2013.07.012

953 Bellahsen, N., Mouthereau, F., Boutoux, A., Bellanger, M., Lacombe, O., Jolivet, L., &
954 Rolland, Y. (2014). Collision kinematics in the western external Alps. Tectonics, 33(6), 1055–
955 1088. https://doi.org/10.1002/2013TC003453

956 Bellanger, M., Bellahsen, N., Jolivet, L., Baudin, T., Augier, R., & Boutoux, A. (2014).
957 Basement shear zones development and shortening kinematics in the Ecrins Massif, Western
958 Alps. Tectonics, 33(2), 84–111. https://doi.org/10.1002/2013TC003294

959 Beltrando, M., Frasca, G., Compagnoni, R., & Vitale-Brovarone, A. (2012). The Valaisan
960 controversy revisited: Multi-stage folding of a Mesozoic hyper-extended margin in the Petit St.
961 Bernard pass area (Western Alps). Tectonophysics, 579, 17–36.
962 https://doi.org/10.1016/J.TECTO.2012.02.010

963 Beltrando, M., Manatschal, G., Mohn, G., Dal Piaz, G. V., Vitale Brovarone, A., &
964 Masini, E. (2014). Recognizing remnants of magma-poor rifted margins in high-pressure
965 orogenic belts: The Alpine case study. Earth-Science Reviews, 131, 88–115.
966 https://doi.org/10.1016/J.EARSCIREV.2014.01.001

967 Bergemann, C., Gnos, E., Berger, A., Janots, E., & Whitehouse, M. J. (2020). Dating
968 tectonic activity in the Lepontine Dome and Rhone-Simplon Fault regions through hydrothermal
969 monazite-(Ce). Solid Earth, 11(1), 199–222. https://doi.org/10.5194/se-11-199-2020

970 Berger, A., Mercolli, I. P., Herwegh, M., & Gnos, E. (2017). Explanatory Notes to the
971 Geological map of the Aar massif, Tavetsch and Gotthard nappes, Geological special map No.
972 129. Wabern: Federal Office of Topography swisstopo.

973 Berger, A., Engi, M., Erne-Schmid, S., Glotzbach, C., Spiegel, C., de Goede, R., &
974 Herwegh, M. (2020). The relation between peak metamorphic temperatures and subsequent
975 cooling during continent–continent collision (western Central Alps, Switzerland). Swiss Journal
976 of Geosciences, 113(1), 1–18. https://doi.org/10.1186/S00015-020-00356-4

977 Bertini, G., Marcucci, M., Nevini, R., Passerini, P., & Sguazzoni, G. (1985). Patterns of
978 faulting in the Mont Blanc granite. Tectonophysics, 111(1–2), 65–106.
979 https://doi.org/10.1016/0040-1951(85)90066-6

Bistacchi, A., Massironi, M., Menegon, L., Bolognesi, F., & Donghi, V. (2012). On the nucleation of non-Andersonian faults along phyllosilicate-rich mylonite belts. Geological Society, London, Special Publications, 367(1), 185-199. https://doi.org/10.1144/SP367.13

Boston, K. R., Rubatto, D., Hermann, J., Engi, M., & Amelin, Y. (2017). Geochronology of accessory allanite and monazite in the Barrovian metamorphic sequence of the Central Alps, Switzerland. Lithos, 286–287, 502–518. https://doi.org/10.1016/J.LITHOS.2017.06.025

Bühler, M., Zurbriggen, R., Berger, A., Herwegh, M., & Rubatto, D. (2022). Late Carboniferous Schlingen in the Gotthard nappe (Central Alps) and their relation to the Variscan evolution. International Journal of Earth Sciences, 1–26. https://doi.org/10.1007/S00531-022-02247-5

Bürgmann, R., & Dresen, G. (2008). Rheology of the lower crust and upper mantle: Evidence from rock mechanics, geodesy, and field observations. Annu. Rev. Earth Planet. Sci., 36, 531-567. https://doi.org/10.1146/annurev.earth.36.031207.124326

Bussien, D., Bussy, F., Masson, H., Magna, T., & Rodionov, N. (2008). Variscan lamprophyres in the Lower Penninic domain (Central Alps): Age and tectonic significance. Bulletin de La Societe Geologique de France, 179(4), 369–381. https://doi.org/10.2113/gssgfbull.179.4.369

Campani, M., Mancktelow, N., Seward, D., Rolland, Y., Müller, W., & Guerra, I. (2010). Geochronological evidence for continuous exhumation through the ductile-brittle transition along a crustal-scale low-angle normal fault: Simplon Fault Zone, central Alps. Tectonics, 29(3). https://doi.org/10.1029/2009TC002582

Candioti, L. G., Duretz, T., Moulas, E., & Schmalholz, S. M. (2021). Buoyancy versus shear forces in building orogenic wedges. Solid Earth, 12(8), 1749–1775. https://doi.org/10.5194/se-12-1749-2021

Ceccato, A., & Pennacchioni, G. (2018). Structural evolution of the Rieserferner pluton in the framework of the Oligo-Miocene tectonics of the Eastern Alps. Journal of Structural Geology, 116, 64-80. https://doi.org/10.1016/j.jsg.2018.08.004

Ceccato, A., Menegon, L., Warren, C. J., & Halton, A. M. (2020). Structural and metamorphic inheritance controls strain partitioning during orogenic shortening (Kalak Nappe Complex, Norwegian Caledonides). Journal of Structural Geology, 136, 104057. https://doi.org/10.1016/j.jsg.2020.104057

Ceccato, A., Goncalves, P., & Menegon, L. (2022). On the petrology and microstructures of small-scale ductile shear zones in granitoid rocks: An overview. Journal of Structural Geology, 161(June), 104667. https://doi.org/10.1016/j.jsg.2022.104667

Ceccato, A., Behr, W. M., Zappone, A. S., Tavazzani, L., Giuliani, A., (2023). Datasets for "Structural evolution, exhumation rates, and rheology of the European crust during Alpine collision: constraints from the Rotondo granite – Gotthard nappe". ETH Zurich Research Collection. DOI 10.3929/ethz-b-000644819

Cesare, B., Nestola, F., Johnson, T., Mugnaioli, E., Della Ventura, G., Peruzzo, L., Bartoli, O., Viti, C. & Erickson, T. (2019). Garnet, the archetypal cubic mineral, grows tetragonal. Scientific Reports, 9(1), 14672. https://doi.org/10.1038/s41598-019-51214-9

Célini, N., Mouthereau, F., Lahfid, A., Gout, C., & Callot, J. P. (2023). Rift thermal inheritance in the SW Alps (France): insights from RSCM thermometry and 1D thermal numerical modelling. Solid Earth, 14(1), 1–16. https://doi.org/10.5194/SE-14-1-2023

Cenki-Tok, B., Darling, J. R., Rolland, Y., Dhuime, B., & Storey, C. D. (2014). Direct dating of mid-crustal shear zones with synkinematic allanite: new in situ U-Th-Pb geochronological approaches applied to the Mont Blanc massif. Terra Nova, 26(1), 29–37. https://doi.org/10.1111/TER.12066

Challandes, N., Marquer, D., & Villa, I. M. (2008). P-T-t modelling, fluid circulation, and 39Ar-40Ar and Rb-Sr mica ages in the Aar Massif shear zones (Swiss Alps). Swiss Journal of Geosciences, 101(2), 269–288. https://doi.org/10.1007/s00015-008-1260-6

Collettini, C., Tesei, T., Scuderi, M. M., Carpenter, B. M., & Viti, C. (2019). Beyond Byerlee friction, weak faults and implications for slip behavior. Earth and Planetary Science Letters, 519, 245-263. https://doi.org/10.1016/j.epsl.2019.05.011

Connolly, J. A. D. (2005). Computation of phase equilibria by linear programming: A tool for geodynamic modeling and its application to subduction zone decarbonation. Earth and Planetary Science Letters, 236(1–2), 524–541. https://doi.org/10.1016/J.EPSL.2005.04.033

Cook, K. L., & Royden, L. H. (2008). The role of crustal strength variations in shaping orogenic plateaus, with application to Tibet. Journal of Geophysical Research: Solid Earth, 113(B8). https://doi.org/10.1029/2007JB005457

Cox, S. F. (2010). The application of failure mode diagrams for exploring the roles of fluid pressure and stress states in controlling styles of fracture-controlled permeability enhancement in faults and shear zones. Geofluids, 10(1–2), 217–233. https://doi.org/10.1111/j.1468-8123.2010.00281.x

Dal Piaz, G. V., Bistacchi, A., & Massironi, M. (2003). Geological outline of the Alps. Episodes, 26(3), 175–180. https://doi.org/https://doi.org/10.18814/epiiugs/2003/v26i3/004

Dall'Asta, N., Hoareau, G., Manatschal, G., Centrella, S., Denèle, Y., Ribes, C., & Kalifi, A. (2022). Structural and petrological characteristics of a Jurassic detachment fault from the Mont-Blanc massif (Col du Bonhomme area, France). Journal of Structural Geology, 159(March). https://doi.org/10.1016/j.jsg.2022.104593

Deng, X.-D., Li, J.-W., Luo, T., and Wang, H.-Q., 2017, Dating magmatic and hydrothermal processes using andradite-rich garnet U–Pb geochronometry. Contributions to Mineralogy and Petrology, v. 172, p. 71, doi:10.1007/s00410-017-1389-2.

Egli, D., Müller, W., & Mancktelow, N. (2016). Laser-cut Rb–Sr microsampling dating of deformational events in the Mont Blanc-Aiguilles Rouges region (European Alps). Terra nova, 28(1), 35-42. https://doi.org/10.1111/ter.12184

Egli, D., Mancktelow, N., & Spikings, R. (2017). Constraints from 40Ar/39Ar geochronology on the timing of Alpine shear zones in the Mont Blanc-Aiguilles Rouges region of the European Alps. Tectonics, 36(4), 730-748. https://doi.org/10.1002/2016TC004450

Etheridge, M. A. (1983). Differential stress magnitudes during regional deformation and metamorphism: Upper bound imposed by tensile fracturing. Geology, 11(4), 231–234. https://doi.org/10.1130/0091-7613(1984)12

Fitzpayne, A., Giuliani, A., Hergt, J., Woodhead, J. D., & Maas, R. (2020). Isotopic analyses of clinopyroxenes demonstrate the effects of kimberlite melt metasomatism upon the lithospheric mantle. Lithos, 370, 105595. https://doi.org/10.1016/j.lithos.2020.105595

Galli, A., Mancktelow, N., Reusser, E., & Caddick, M. (2007). Structural geology and petrography of the Naret region (northern Valle Maggia, N.Ticino, Switzerland). Swiss Journal of Geosciences, 100(1), 53–70. https://doi.org/10.1007/s00015-007-1211-7

Gapais, D., Bale, P., Choukroune, P., Cobbold, P. R., Mahjoub, Y., & Marquer, D. (1987). Bulk kinematics from shear zone patterns: some field examples. Journal of Structural Geology, 9(5–6), 635–646. https://doi.org/10.1016/0191-8141(87)90148-9

Girault, J. B., Bellahsen, N., Boutoux, A., Rosenberg, C. L., Nanni, U., Verlaguet, A., & Beyssac, O. (2020). The 3-D Thermal Structure of the Helvetic Nappes of the European Alps: Implications for Collisional Processes. Tectonics, 39(3), e2018TC005334. https://doi.org/10.1029/2018TC005334

Giuliani, A., Guillong, M., Maas, R., & Howarth, G. H. (2023). In-situ Rb-Sr dating of mica without employing the MicaMG standard. In Goldschmidt 2023 Conference. GOLDSCHMIDT. https://doi.org/10.7185/gold2023.20131

Glotzbach, C., Reinecker, J., Danišík, M., Rahn, M., Frisch, W., & Spiegel, C. (2010). Thermal history of the central Gotthard and Aar massifs, European Alps: Evidence for steady state, long-term exhumation. Journal of Geophysical Research: Earth Surface, 115(F3). https://doi.org/10.1029/2009JF001304

Goncalves, P., Oliot, E., Marquer, D., & Connolly, J. A. D. (2012). Role of chemical processes on shear zone formation: An example from the grimsel metagranodiorite (Aar massif, Central Alps). Journal of Metamorphic Geology, 30(7), 703–722. https://doi.org/10.1111/j.1525-1314.2012.00991.x

Goncalves, P., Poilvet, J. C., Oliot, E., Trap, P., & Marquer, D. (2016). How does shear zone nucleate? An example from the Suretta nappe (Swiss Eastern Alps). Journal of Structural Geology, 86, 166–180. https://doi.org/10.1016/j.jsg.2016.02.015

Green, E., Holland, T., & Powell, R. (2007). An order-disorder model for omphacitic pyroxenes in the system jadeite-diopside-hedenbergite-acmite, with applications to eclogitic rocks. American Mineralogist, 92(7), 1181–1189. https://doi.org/10.2138/AM.2007.2401

Groome, W. G., Koons, P. O., & Johnson, S. E. (2008). Metamorphism, transient mid-crustal rheology, strain localization and the exhumation of high-grade metamorphic rocks. Tectonics, 27(1). https://doi.org/10.1029/2006TC001992

Guermani, A., & Pennacchioni, G. (1998). Brittle precursors of plastic deformation in a granite: An example from the Mont Blanc massif (Helvetic, western Alps). Journal of Structural Geology, 20(2–3), 135–148. https://doi.org/10.1016/S0191-8141(97)00080-1

Guillong, M., Hametner, K., Reusser, E., Wilson, S. A., & Günther, D. (2005). Preliminary characterisation of new glass reference materials (GSA-1G, GSC-1G, GSD-1G and GSE-1G) by laser ablation-inductively coupled plasma-mass spectrometry using 193 nm, 213 nm and 266 nm wavelengths. Geostandards and Geoanalytical Research, 29(3), 315-331. https://doi.org/10.1111/j.1751-908X.2005.tb00903.x

Guillong, M., von Quadt, A., Sakata, S., Peytcheva, I., & Bachmann, O. (2014). LA-ICP-MS Pb–U dating of young zircons from the Kos–Nisyros volcanic centre, SE Aegean arc. J. Anal. At. Spectrom., 29(6), 963–970. https://doi.org/10.1039/C4JA00009A

Hafner, S. (1958). Petrographie des südwestlichen Gotthardmassives (zwischen St. Gotthardpass und Nufenenpass). Schweizerische Mineralogische und Petrographische Mitteilungen (Vol. 38). https://doi.org/10.3929/ethz-a-000097546

Handy, M. R., M. Schmid, S., Bousquet, R., Kissling, E., & Bernoulli, D. (2010). Reconciling plate-tectonic reconstructions of Alpine Tethys with the geological-geophysical record of spreading and subduction in the Alps. Earth-Science Reviews, 102(3–4), 121–158. https://doi.org/10.1016/j.earscirev.2010.06.002

Hentschel, F., Janots, E., Trepmann, C. A., Magnin, V., & Lanari, P. (2020). Corona formation around monazite and xenotime during greenschist-facies metamorphism and deformation. European Journal of Mineralogy, 32(5), 521-544. https://doi.org/10.5194/ejm-32-521-2020

Herwegh, M., Berger, A., Baumberger, R., Wehrens, P., & Kissling, E. (2017). Large-Scale Crustal-Block-Extrusion During Late Alpine Collision. Scientific Reports, 7(1), 1–10. https://doi.org/10.1038/s41598-017-00440-0

Herwegh, M., Berger, A., Glotzbach, C., Wangenheim, C., Mock, S., Wehrens, P., et al. (2020). Late stages of continent-continent collision: Timing, kinematic evolution, and exhumation of the Northern rim (Aar Massif) of the Alps. Earth-Science Reviews, 200, 102959. https://doi.org/10.1016/J.EARSCIREV.2019.102959

Hogmalm K. J., Zack T., Karlsson A. K. O., Sjöqvist A. S. L. and Garbe-Schönberg D. (2017) In situ Rb–Sr and K–Ca dating by LA-ICP-MS/MS: an evaluation of N2O and SF6 as reaction gases. Journal of Analytical Atomic Spectrometry 32, 305-313. DOI:10.1039/C6JA00362A

Holland, T. J. B., & Powell, R. (1998). An internally consistent thermodynamic data set for phases of petrological interest. Journal of Metamorphic Geology, 16(3), 309–343. https://doi.org/10.1111/J.1525-1314.1998.00140.X

Holland, T. J. B., & Powell, R. (2011). An improved and extended internally consistent thermodynamic dataset for phases of petrological interest, involving a new equation of state for solids. Journal of Metamorphic Geology, 29(3), 333–383. https://doi.org/10.1111/J.1525-1314.2010.00923.X

Horstwood, M.S.A., Košler, J., Gehrels, G., Jackson, S.E., McLean, N.M., Paton, C., Pearson, N.J., Sircombe, K., Sylvester, P., Vermeesch, P., Bowring, J.F., Condon, D.J., Schoene, B., 2016. Community-Derived Standards for LA - ICP - MS U-(Th-)Pb Geochronology – Uncertainty Propagation, Age Interpretation and Data Reporting. Geostand Geoanal Res 40, 311–332. https://doi.org/10.1111/j.1751-908X.2016.00379.x

Jamtveit, B., Petley-Ragan, A., Incel, S., Dunkel, K. G., Aupart, C., Austrheim, H., Corfu, F., Menegon, L. & Renard, F. (2019). The effects of earthquakes and fluids on the metamorphism of the lower continental crust. Journal of Geophysical Research: Solid Earth, 124(8), 7725-7755. https://doi.org/10.1029/2018JB016461

1144 Janots, E., & Rubatto, D. (2014). U-Th-Pb dating of collision in the external Alpine
1145 domains (Urseren zone, Switzerland) using low temperature allanite and monazite. Lithos, 184–
1146 187, 155–166. https://doi.org/10.1016/j.lithos.2013.10.036

1147 Janots, E., Engi, M., Berger, A., Allaz, J., Schwarz, J. O., & Spandler, C. (2008).
1148 Prograde metamorphic sequence of REE minerals in pelitic rocks of the Central Alps:
1149 Implications for allanite-monazite-xenotime phase relations from 250 to 610°C. Journal of
1150 Metamorphic Geology, 26(5), 509–526. https://doi.org/10.1111/j.1525-1314.2008.00774.x

1151 Janots, E., Engi, M., Rubatto, D., Berger, A., Gregory, C., & Rahn, M. (2009).
1152 Metamorphic rates in collisional orogeny from in situ allanite and monazite dating. Geology,
1153 37(1), 11–14. https://doi.org/10.1130/G25192A.1

1154 Jébrak, M. (1997). Hydrothermal breccias in vein-type ore deposits: A review of
1155 mechanisms, morphology and size distribution. Ore Geology Reviews, 12(3), 111–134.
1156 https://doi.org/10.1016/S0169-1368(97)00009-7

1157 Jenkin, G. R., Ellam, R. M., Rogers, G., & Stuart, F. M. (2001). An investigation of
1158 closure temperature of the biotite Rb-Sr system: The importance of cation exchange. Geochimica
1159 et Cosmochimica Acta, 65(7), 1141-1160. https://doi.org/10.1016/S0016-7037(00)00560-3

1160 Kralik, M., Clauer, N., Holnsteiner, R., Huemer, H., & Kappel, F. (1992). Recurrent fault
1161 activity in the Grimsel Test Site (GTS, Switzerland) : revealed by Rb-Sr, K-Ar and tritium
1162 isotope techniques. Journal - Geological Society (London), 149(2), 293–301.
1163 https://doi.org/10.1144/GSJGS.149.2.0293

1164 Lacombe, O., & Mouthereau, F. (2002). Basement-involved shortening and deep
1165 detachment tectonics in forelands of orogens: Insights from recent collision belts (Taiwan,
1166 Western Alps, Pyrenees). Tectonics, 21(4), 12-1. https://doi.org/10.1029/2001TC901018

1167 Lemoine, M., Bas, T., Arnaud-Vanneau, A., Arnaud, H., Dumont, T., Gidon, M., et al.
1168 (1986). The continental margin of the Mesozoic Tethys in the Western Alps. Marine and
1169 Petroleum Geology, 3(3), 179–199. https://doi.org/10.1016/0264-8172(86)90044-9

1170 Leydier, T., Goncalves, P., Lanari, P., & Oliot, E. (2019). On the petrology of brittle
1171 precursors of shear zones – An expression of concomitant brittle deformation and fluid–rock
1172 interactions in the 'ductile' continental crust? Journal of Metamorphic Geology, 37(8), 1129–
1173 1149. https://doi.org/10.1111/jmg.12504

1174 Lützenkirchen, V., & Loew, S. (2011). Late Alpine brittle faulting in the Rotondo granite
1175 (Switzerland): Deformation mechanisms and fault evolution. Swiss Journal of Geosciences,
1176 104(1), 31–54. https://doi.org/10.1007/s00015-010-0050-0

1177 Ma, X., Hertrich, M., Amann, F., Bröker, K., Doonechaly, N. G., Gischig, V., et al.
1178 (2022). Multi-disciplinary characterizations of the BedrettoLab-A new underground geoscience
1179 research facility. Solid Earth, 13(2), 301–322. https://doi.org/10.5194/se-13-301-2022

1180 Mancktelow, N., & Pennacchioni, G. (2010). Why calcite can be stronger than quartz.
1181 Journal of Geophysical Research: Solid Earth, 115(10), 1–16.
1182 https://doi.org/10.1029/2009JB006526

1183 Mancktelow, N., & Pennacchioni, G. (2020). Intermittent fracturing in the middle
1184 continental crust as evidence for transient switching of principal stress axes associated with the

subduction zone earthquake cycle. Geology, 48(11), 1072–1076. https://doi.org/10.1130/G47625.1

McDonough, W. F., & Sun, S. S. (1995). The composition of the Earth. Chemical geology, 120(3-4), 223-253. https://doi.org/10.1016/0009-2541(94)00140-4

Melosh, B. L., Rowe, C. D., Smit, L., Groenewald, C., Lambert, C. W., & Macey, P. (2014). Snap, Crackle, Pop: Dilational fault breccias record seismic slip below the brittle–plastic transition. Earth and Planetary Science Letters, 403, 432-445. https://doi.org/10.1016/j.epsl.2014.07.002

Menegon, L., & Pennacchioni, G. (2010). Local shear zone pattern and bulk deformation in the Gran Paradiso metagranite (NW Italian Alps). International Journal of Earth Sciences, 99(8), 1805–1825. https://doi.org/10.1007/S00531-009-0485-6

Menegon, L., Nasipuri, P., Stünitz, H., Behrens, H., & Ravna, E. (2011). Dry and strong quartz during deformation of the lower crust in the presence of melt. Journal of Geophysical Research: Solid Earth, 116(B10). https://doi.org/10.1029/2011JB008371

Mohn, G., Manatschal, G., Beltrando, M., & Haupert, I. (2014). The role of rift-inherited hyper-extension in Alpine-type orogens. Terra Nova, 26(5), 347-353. https://doi.org/10.1111/ter.12104

Mouthereau, F., Watts, A. B., & Burov, E. (2013). Structure of orogenic belts controlled by lithosphere age. Nature geoscience, 6(9), 785-789. https://doi.org/10.1038/ngeo1902

Musso Piantelli, F., Mair, D., Berger, A., Schlunegger, F., Wiederkehr, M., Kurmann, E., et al. (2022). 4D reconstruction of the Doldenhorn nappe-basement system in the Aar massif: Insights into late-stage continent-continent collision in the Swiss Alps. Tectonophysics, 843, 229586. https://doi.org/10.1016/J.TECTO.2022.229586

Newton, R. C., Charlu, T. V., & Kleppa, O. J. (1980). Thermochemistry of the high structural state plagioclases. Geochimica et Cosmochimica Acta. https://doi.org/10.1016/0016-7037(80)90283-5

Nibourel, L., Berger, A., Egli, D., Heuberger, S., & Herwegh, M. (2021). Structural and thermal evolution of the eastern Aar Massif: insights from structural field work and Raman thermometry. Swiss Journal of Geosciences, 114(1). https://doi.org/10.1186/s00015-020-00381-3

Oliot, E., Goncalves, P., & Marquer, D. (2010). Role of plagioclase and reaction softening in a metagranite shear zone at mid-crustal conditions (Gotthard Massif, Swiss Central Alps). Journal of Metamorphic Geology, 28(8), 849–871. https://doi.org/10.1111/j.1525-1314.2010.00897.x

Oliot, E., Goncalves, P., Schulmann, K., Marquer, D., & Lexa, O. (2014). Mid-crustal shear zone formation in granitic rocks: Constraints from quantitative textural and crystallographic preferred orientations analyses. Tectonophysics, 612–613, 63–80. https://doi.org/10.1016/j.tecto.2013.11.032

Paton, C., Hellstrom, J., Paul, B.,Woodhead, J. and Hergt, J. (2011) Iolite: Freeware for the visualisation and processing of mass spectrometric data. Journal of Analytical Atomic Spectrometry. doi:10.1039/c1ja10172b.

Pennacchioni, G., Di Toro, G., Brack, P., Menegon, L., & Villa, I. M. (2006). Brittle–ductile–brittle deformation during cooling of tonalite (Adamello, Southern Italian Alps). Tectonophysics, 427(1-4), 171-197. https://doi.org/10.1016/j.tecto.2006.05.019

Pennacchioni, G., Ceccato, A., Fioretti, A. M., Mazzoli, C., Zorzi, F., & Ferretti, P. (2016). Episyenites in meta-granitoids of the Tauern Window (Eastern Alps): unpredictable? Journal of Geodynamics, 101, 73–87. https://doi.org/10.1016/j.jog.2016.04.001

Pfiffner, O. A. (2016). Basement-involved thin-skinned and thick-skinned tectonics in the Alps. Geological Magazine, 153(5-6), 1085-1109. doi:10.1017/S0016756815001090

Piccolo, A., Faccenda, M., Carosi, R., Montomoli, C., & Visonà, D. (2018). Crustal strength control on structures and metamorphism in collisional orogens. Tectonophysics, 746, 470-492. https://doi.org/10.1016/j.tecto.2017.09.018

Pleuger, J., Mancktelow, N., Zwingmann, H., & Manser, M. (2012). K–Ar dating of synkinematic clay gouges from Neoalpine faults of the Central, Western and Eastern Alps. Tectonophysics, 550–553, 1–16. https://doi.org/10.1016/J.TECTO.2012.05.001

Pozzi, G., Scuderi, M. M., Tinti, E., Nazzari, M., & Collettini, C. (2022). The role of fault rock fabric in the dynamics of laboratory faults. Journal of Geophysical Research: Solid Earth, 127(6), e2021JB023779. https://doi.org/10.1029/2021JB023779

Redaa A., Farkaš J., Gilbert S., Collins A. S., Wade B., Löhr S., Zack T. & Garbe-Schönberg D. (2021) Assessment of elemental fractionation and matrix effects during in situ Rb–Sr dating of phlogopite by LA-ICP-MS/MS: implications for the accuracy and precision of mineral ages. Journal of Analytical Atomic Spectrometry 36, 322-344. DOI: https://doi.org/10.1039/D0JA00299B

Redaa A., Farkaš J., Gilbert S., Collins A. S., Löhr S., Vasegh D., Forster M., Blades M., Zack T., Giuliani A., Maas R., Baldermann A., Dietzel M. & Garbe-Schönberg D. (2023) Testing Nano-Powder and Fused-Glass Mineral Reference Materials for In Situ Rb-Sr Dating of Glauconite, Phlogopite, Biotite and Feldspar via LA-ICP-MS/MS. Geostandards and Geoanalytical Research 47, 23-48.https://doi.org/10.1111/ggr.12467

Ribeiro, B. V., Kirkland, C. L., Kelsey, D. E., Reddy, S. M., Hartnady, M. I., Faleiros, F. M., ... & Clark, C. (2023). Time-strain evolution of shear zones from petrographically constrained Rb–Sr muscovite analysis. Earth and Planetary Science Letters, 602, 117969. https://doi.org/10.1016/j.epsl.2022.117969

Rast, M., Galli, A., Ruh, J. B., Guillong, M., & Madonna, C. (2022). Geology along the Bedretto tunnel: kinematic and geochronological constraints on the evolution of the Gotthard Massif (Central Alps). Swiss Journal of Geosciences, 115(1). https://doi.org/10.1186/s00015-022-00409-w

Ricchi, E., Bergemann, C., Gnos, E., Berger, A., Rubatto, D., & Whitehouse, M. J. (2019). Constraining deformation phases in the Aar Massif and the Gotthard Nappe (Switzerland) using Th-Pb crystallization ages of fissure monazite-(Ce). Lithos, 342–343, 223–238. https://doi.org/10.1016/J.LITHOS.2019.04.014

Rolland, Y., & Rossi, M. (2016). Two-stage fluid flow and element transfers in shear zones during collision burial-exhumation cycle: Insights from the Mont Blanc Crystalline Massif (Western Alps). Journal of Geodynamics, 101, 88-108. https://doi.org/10.1016/j.jog.2016.03.016

Rolland, Y., Rossi, M., Cox, S. F., Corsini, M., Mancktelow, N., Pennacchioni, G., et al. (2008). 40Ar/39Ar dating of synkinematic white mica: Insights from fluid-rock reaction in low-grade shear zones (Mont Blanc Massif) and constraints on timing of deformation in the NW external Alps. Geological Society Special Publication, 299, 293–315. https://doi.org/10.1144/SP299.18

Rolland, Y., Cox, S. F., & Corsini, M. (2009). Constraining deformation stages in brittle-ductile shear zones from combined field mapping and 40Ar/39Ar dating: The structural evolution of the Grimsel Pass area (Aar Massif, Swiss Alps). Journal of Structural Geology, 31(11), 1377–1394. https://doi.org/10.1016/j.jsg.2009.08.003

Rosenberg, C. L., & Kissling, E. (2013). Three-dimensional insight into Central-Alpine collision: Lower-plate or upper-plate indentation? Geology, 41(12), 1219–1222. https://doi.org/10.1130/G34584.1

Rosenberg, C. L., Bellahsen, N., Rabaute, A., & Girault, J. B. (2021). Distribution, style, amount of collisional shortening, and their link to Barrovian metamorphism in the European Alps. Earth-Science Reviews, 222, 103774. https://doi.org/10.1016/j.earscirev.2021.103774

Rubatto, D., Hermann, J., Berger, A., & Engi, M. (2009). Protracted fluid-induced melting during Barrovian metamorphism in the Central Alps. Contributions to Mineralogy and Petrology, 158, 703-722. https://doi.org/10.1007/s00410-009-0406-5

Sanchez, G., Rolland, Y., Schneider, J., Corsini, M., Oliot, E., Goncalves, P., Verati, C., Lardeaux, J.M. & Marquer, D. (2011). Dating low-temperature deformation by 40Ar/39Ar on white mica, insights from the Argentera-Mercantour Massif (SW Alps). Lithos, 125(1–2), 521–536. https://doi.org/10.1016/J.LITHOS.2011.03.009

Sarkar, S., Giuliani, A., Dalton, H., Phillips, D., Ghosh, S., Misev, S., & Maas, R. (2023). Derivation of Lamproites and Kimberlites from a Common Evolving Source in the Convective Mantle: the Case for Southern African 'Transitional Kimberlites'. Journal of Petrology, 64(7), egad043. https://doi.org/10.1093/petrology/egad043

Schmid, S. M., Fügenschuh, B., Kissling, E., & Schuster, R. (2004). Tectonic map and overall architecture of the Alpine orogen. Eclogae Geologicae Helvetiae, 97(1), 93–117. https://doi.org/10.1007/S00015-004-1113-X

Seman, S., Stockli, D.F., and McLean, N.M., 2017, U-Pb geochronology of grossular-andradite garnet: Chemical Geology, v. 460, p. 106–116, doi:10.1016/j.chemgeo.2017.04.020.

Sibson, R. H. (1985). Stopping of earthquake ruptures at dilational fault jogs. Nature, 316(6025), 248-251. https://doi.org/10.1038/316248a0

Sibson, R. H. (1987). Earthquake rupturing as a mineralizing agent in hydrothermal systems. Geology, 15(8), 701-704. https://doi.org/10.1130/0091-7613(1987)15%3C701:ERAAMA%3E2.0.CO;2

Sibson, R. H. (2003). Brittle-failure controls on maximum sustainable overpressure in different tectonic regimes. American Association of Petroleum Geologists Bulletin, 87(6), 901–908. https://doi.org/10.1306/01290300181

Sibson, R. H., Robert, F., & Poulsen, K. H. (1988). High-angle reverse faults, fluid-pressure cycling, and mesothermal gold-quartz deposits. Geology, 16(June), 551–555. https://doi.org/doi.org/10.1130/0091-7613(1988)016%3C0551:HARFFP%3E2.3.CO;2

Simonetti, M., Carosi, R., Montomoli, C., Cottle, J. M., & Law, R. D. (2020). Transpressive Deformation in the Southern European Variscan Belt: New Insights From the Aiguilles Rouges Massif (Western Alps). Tectonics, 39(6), e2020TC006153. https://doi.org/10.1029/2020TC006153

Spear, F. S. (2010). Monazite–allanite phase relations in metapelites. Chemical Geology, 279(1-2), 55-62. https://doi.org/10.1016/j.chemgeo.2010.10.004

Steck, A. (1976). Albit-Oligoklas-Mineralgesellschaften der Peristeritlücke aus alpinmetamorphen Granitgneisen des Gotthardmassivs. Schweizerische Mineralogische Und Petrographische Mitteilungen, 56, 269–292. https://doi.org/10.5169/seals-43687

Steck, A., & Burri, G. (1971). Chemismus und Paragenesen von Granaten aus Granitgneisen der Grünschiefer- und Amphiholitfazies der Zentralalpen. Schweizerische Mineralogische Und Petrographische Mitteilungen, 51(2–3), 534–538.

Vanardois, J., Trap, P., Roger, F., Melleton, J., Marquer, D., Paquette, J. L., Goncalves, P., Cagnard, F., & Le Bayon, B. (2022). Deformation, crustal melting and magmatism in the crustal-scale East-Variscan Shear Zone (Aiguilles-Rouges and Mont-Blanc massifs, Western Alps). Journal of Structural Geology, 163, 104724. https://doi.org/10.1016/J.JSG.2022.104724

Vermeesch, P. (2018). IsoplotR: A free and open toolbox for geochronology. Geoscience Frontiers, 9(5), 1479-1493. https://doi.org/10.1016/j.gsf.2018.04.001

Vogt, K., Willingshofer, E., Matenco, L., Sokoutis, D., Gerya, T., & Cloetingh, S. (2018). The role of lateral strength contrasts in orogenesis: A 2D numerical study. Tectonophysics, 746, 549–561. https://doi.org/10.1016/J.TECTO.2017.08.010

Volpe, G., Pozzi, G., & Collettini, C. (2022). YBPR or SCC′? Suggestion for the nomenclature of experimental brittle fault fabric in phyllosilicate-granular mixtures. Journal of Structural Geology, 165, 104743. https://doi.org/10.1016/j.jsg.2022.104743

Volpe, G., Pozzi, G., Collettini, C., Spagnuolo, E., Achtziger-Zupančič, P., Zappone, A., Aldega, L., Meier, M.A., Giardini, D., & Cocco, M. (2023). Laboratory simulation of fault reactivation by fluid injection and implications for induced seismicity at the BedrettoLab, Swiss Alps. Tectonophysics, 862, 229987. https://doi.org/10.1016/j.tecto.2023.229987

Waldbaum, D. R., & Thompson Jr., J. B. (1968). Mixing properties of sanidine crystalline solutions; [Part] 2, Calculations based on volume data. American Mineralogist.

Wehrens, P., Berger, A., Peters, M., Spillmann, T., & Herwegh, M. (2016). Deformation at the frictional-viscous transition: Evidence for cycles of fluid-assisted embrittlement and ductile deformation in the granitoid crust. Tectonophysics, 693, 66–84. https://doi.org/10.1016/j.tecto.2016.10.022

Weisenberger, T., & Bucher, K. (2010). Zeolites in fissures of granites and gneisses of the Central Alps. Journal of Metamorphic Geology, 28(8), 825–847. https://doi.org/10.1111/J.1525-1314.2010.00895.X

White, R. W., Powell, R., Holland, T. J. B., Johnson, T. E., & Green, E. C. R. (2014). New mineral activity–composition relations for thermodynamic calculations in metapelitic systems. Journal of Metamorphic Geology, 32(3), 261–286. https://doi.org/10.1111/JMG.12071

Whitney, D. L., & Evans, B. W. (2010). Abbreviations for names of rock-forming minerals. American Mineralogist, 95(1), 185–187. https://doi.org/10.2138/am.2010.3371

Wiederkehr, M., Bousquet, R., Ziemann, M. A., Berger, A., & Schmid, S. M. (2011). 3-D assessment of peak-metamorphic conditions by Raman spectroscopy of carbonaceous material: An example from the margin of the Lepontine dome (Swiss Central Alps). International Journal of Earth Sciences, 100(5), 1029–1063. https://doi.org/10.1007/S00531-010-0622-2

Willingshofer, E., Sokoutis, D., & Burg, J. P. (2005). Lithospheric-scale analogue modelling of collision zones with a pre-existing weak zone. Geological Society, London, Special Publications, 243(1), 277-294. https://doi.org/10.1144/GSL.SP.2005.243.01.18

Wolf, S. G., Huismans, R. S., Braun, J., & Yuan, X. (2022). Topography of mountain belts controlled by rheology and surface processes. Nature, 606(7914), 516-521. https://doi.org/10.1038/s41586-022-04700-6

Zertani, S., Menegon, L., Pennacchioni, G., Buisman, I., Corfu, F., & Jamtveit, B. (2023). Protracted localization of metamorphism and deformation in a heterogeneous lower-crustal shear zone. Journal of Structural Geology, 104960. https://doi.org/10.1016/j.jsg.2023.104960